NAZARBAYEV
UNIVERSITY
School of Engineering and Digital Sciences

Bachelor of Engineering in
Mechanical and Aerospace Engineering

Investigation of rheological properties of stainless-steel powder and mechanical performances of SLM printed parts.

(Final Capstone Project Report)

by

Dilnaz Yuldasheva, Alan Ospanov, and Guldariya Zharkynbekova

Lead Supervisor: Prof. Didier Talamona
Co-Supervisor: Prof. Asma Perveen

April, 2024

Declaration

We, Dilnaz Yuldasheva, Alan Ospanov, and Guldariya Zharkynbekova, hereby declare that this report, entitled “Investigation of rheological properties of stainless-steel powder and mechanical performances of SLM printed parts.” is the result of our own project work except for quotations and citations which have been duly acknowledged. We also declare that it has not been previously or concurrently submitted for any other degree at Nazarbayev University or elsewhere.

Signature:

Name:
Alan Ospanov
Dilnaz Yuldasheva
Guldariya Zharkynbekova
Date: April 28, 2024

Acknowledgments

This research was supported in part by the Research Grant OP2023004 from Nazarbayev University.

Abstract

This study focuses on the rheological properties of the atomized stainless-steel powder and the mechanical performances of the specimens obtained by selective laser melting (SLM). Rheological properties of atomized stainless-steel powders provided by two suppliers were characterized using the FT4 Rheometer, scanning electron microscopy (SEM), Hall flowmeter, Tap density measurer, and the Mastersizer 3000. The mechanical performance of the SLM printed specimens was investigated with the help of tensile, fatigue, hardness, and corrosion tests. This study provides a characterization of the influence of the build orientation and heat treatment on mechanical properties of SLM printed parts. Additionally, a literature review was prepared for the current state of research on each of the relevant properties of SLM printed 316L stainless steel parts. These comprehensive quantitative and qualitative analyses are beneficial to anticipate the failure conditions of stainless-steel specimens. From the rheological analysis, it was observed that the atomized powder provided by supplier 1 had better flowability and rheological properties. However, it was found that both commercial powders were deemed free-flowing and sufficiently appropriate for 3D printing, which is why a mixture of both was used in this study. Build orientation was found to have an effect on fatigue, hardness, and corrosion properties, while tensile performance was not significantly affected. Additionally, SEM imaging revealed a presence of defects, such as lack of fusion, voids, and unmelted powder particles in as-built specimens. Heat treatment proved to mitigate the number of defects present, leading to noticeable improvements in the properties of SLM printed parts. However, a negative effect was noted for the corrosion resistance, stemming from the increase of the number of grain boundaries, which are most susceptible to corrosion.

Contents

List of Figures

List of Tables

Chapter 1: Introduction

1.1 Research background

Additive manufacturing (AM) is an industrial process of creating objects, layer by layer, relying on three-dimensional modeling data. Metal additive manufacturing focuses on the use of atomized metal powder as building blocks of the 3D printed objects. In the recent years, the core objectives of industrial technology development have been to reduce costs and increase flexibility, AM has gained attention, because it allows the creation of components with complex shapes. In addition, employing AM when creating single parts with complicated shapes is financially sound, because traditionally utilized methods require multiple manufacturing techniques that can be replaced with a single use of AM. The metal additive manufacturing market has a significant impact beyond its direct domain by enabling rapid prototyping and the production of lightweight components. Over the years, various industries have realized the potential benefits of additive technologies and integrated them into their manufacturing processes. Today, an increasing number of companies in sectors such as aerospace, automotive, mechanical engineering, oil and gas, medical, and jewelry are leveraging the immense potential of these innovative techniques. One of the popular technologies of additive manufacturing, or 3D printing, is selective laser melting (SLM). This technique enables the creation of intricate shapes by using a laser to melt the material. The process involves depositing the material layer-by-layer using computer-aided design (CAD) models. A scanning laser beam of high energy density swiftly melts and solidifies the powder particles, which have been placed, to form the desired shapes. Currently, SLM process commonly employs stainless steel (SS) 316L as its primary alloy due to its versatility in various industries such as food and chemical, petrochemical and mechanical engineering, construction, and complex equipment development. This material is known for its exceptional resistance to harsh environments and long-lasting durability. Its protective layer has remarkable stability, and any physical or chemical damage can be easily restored to its original state without compromising its anti-corrosion properties. Furthermore, its high tensile strength and hardness properties make it a vital component for various applications. These properties can be influenced by SLM printing parameters as 3D printing precisely controls the microstructure of the printed material, which affects its mechanical properties. Layer-by-layer deposition enables the creation of structures that optimize strength and other performance characteristics. The properties of stainless steel 316L can be influenced by the parameters of the SLM printing process, as 3D printing allows precise control over the microstructure of the printed material. This control affects mechanical properties, enabling the creation of structures optimized for strength and other performance characteristics. The characteristics of the powder used in the SLM process, including packing density, size distribution, and morphology, directly impact the mechanical properties of the built parts. Spherical powder particles are preferred, as their shape influences the quality of additively manufactured samples. Studies have demonstrated that inhomogeneities in the powder layer can result in micro-structural defects, subsequently affecting part properties like fatigue behavior [3].

This study will give an in depth understanding of the mentioned mechanical properties of SLM printed parts and analyze how processing parameters are affected by the material characteristics.

1.2 Aims and objectives

This work focuses on how the printability parameters and heat treatment of selective laser melting (SLM) are influenced to the mechanical characteristics of stainless steel 316L. The main two goals are to:

1. Investigate the stainless steel 316L powder for SLM printability:

- Rheological properties
- SEM analysis
- Mastersizer particle size distribution

2. Investigate the influence of build direction and heat treatment on the mechanical performance and corrosion behavior:

- Fatigue and tensile testing
- Corrosion testing
- Hardness testing

1.3 Outline

The main purpose of the capstone project is to provide a well-structured and organized framework that explains how the packing density, size distribution, and morphology of the powder contribute to the mechanical properties of the built parts, such as tensile strength, fatigue strength, and other relevant characteristics. The report is organized as follows:

Chapter 1 describes the overview of additive manufacturing, the advantages of SLM printed samples, and the objectives of the research.

Chapter 2 provides background information and previous studies of rheological and mechanical properties of stainless steel 316L such as hardness, tensile, and other properties.

Chapter 3 demonstrates the material preparation, including the powder suppliers and dimensions for printed parts. It also describes techniques and equipment used in the evaluation of tensile, fatigue, hardness, and corrosion rate of stainless steel 316L.

Chapter 4 presents the obtained results of rheological and mechanical tests and compares the values between different angles of direction. The mechanical and electrochemical performance of stainless steel 316L is compared between specimens that have undergone heat treatment and those that are in their as-built state.

Chapter 5 gives the optimized results of fatigue cycles and hardness, tensile strength and corrosion rate for each angle of build direction. It also summarizes how constant parameters of SLM printing are related to the results of measurements.

Chapter 2: Literature review

2.1 Powder preparation methods

The preparation of powders in additive manufacturing has several processes, such as: gas atomization (GA), plasma atomized wire (PAW), induction melted bar atomization (EIGA), and plasma rotating electrode atomization (PREP) and other. GA involves molten metal being dispersed by atomization gas to form spherical particles, ideal for free-flowing powders [4]. In PAW process, plasma streams are produced by dissociation process and gives a variety of powder sizes from fine to coarse with good flowability [5]. Based on recent studies, powder shapes are more spherical for the EIGA process than other atomization types and the presence of satellite particles is a common phenomenon[6]. Additionally, powder atomization by PREP allows it to produce uniform spherical particles without impurities; however, certain metals are not suitable for PREP due to reaction with plasma [7].

This study uses commercial powders produced by gas atomization and plasma rotating electrode process, creating a need to analyze the differences in processes. More detailed information for each techniques is given in Table 2.1.

Moreover, particle size distribution (PSD) is often used to compare atomized powders according to their flowability. Particle size is mainly categorized into fine, medium, and coarse. Based on literature review, coarse particles yield better flowability compared to finer ones [8]. Based on the findings, PREP and GA produce powders with similar PSD [9].

Particle morphology is another important physical property of powder that determines the surface roughness and sphericity of the particle. For all AM technologies, spherical particles with a smooth surface finish are generally preferable because they reduce the packing of the powder and ease the powder flow [12]. Regarding the powder fabricating techniques, results have proven that powder produced by plasma atomization has higher spherical particles than the ones produced by gas atomization. Consequently, it can be said that samples taken from plasma atomization methods show better flowability since more spherical powders have lower surface friction and pack easily which leads to a consistent flow and homogeneous concentration [13].

Table 2.1: Literature review on powder production techniques

Manufacturing process	**Material used**	**Advantages**	**Limitation**
Gas atomization (GA).	316L austenitic stainless steel powders [10].	Argon atomized powders give more spherical morphologies and improved flow properties	There is internal porosity in the powders that can lead to uncertainty of packing properties.
Plasma atomization (PA).	Micron-sized spherical stainless steel powders.[11].	The internal porosity can be avoided by thermal plasma treatment.	There can be hollow powders produced due to high plasma temperature and gas pressure, and the feedstock is commonly in form of wire.
Plasma rotating electrode atomization (PREP).	Ti-6Al-4V, 316-Steel and Co-Cr-Mo alloy [11].	The process gives more spherical powders with better flowability and narrower particle size distributions.	The presence of satellite powder is more likely to occur due to high thermal conductivity of alloys that reduces the flowability of the powders.
Induction melted bar atomization (EIGA)	Ni-based superalloy[6].	It can prepare ultra-clean metal powders as the molten flow remains isolated.	The powder sphericity is varied for four atomization pressures and its flowability decreases.

2.2 Rheological properties of the powder

To obtain a final part by AM without porosity and with a smooth surface, the consistency of the powder must be homogeneous and the flow must be continuous. Powder characteristics such as particle size, shape, bulk density, and angle of repose determine its flowability.

Particle size distribution: Particle size distribution (PSD) plays an important role in powder flowability since interparticle friction depends on the particle size. Powder with a wider size distribution shows more efficient packing and provides parts with a smoother side surface finish [13]. Because wide PSD refers to the presence of both small and coarse particles, which means that small particles most likely can fill the empty spaces between bigger ones [14]. Finer particles have an enhanced tendency to agglomerate due to interparticle forces such as van der Waals forces and gravitational forces, compared to coarser particles [15].

Bulk density: The bulk density can be defined as the fraction of powder mass to the volume, and the volume contains free spaces between particles. There are two types of bulk density: apparent (aerated) bulk density and tapped bulk density. The apparent bulk density of the powder, also known as random loose packing, describes the powder that is dispersed only by the gravitational force [16]. High interparticle friction is commonly observed in powders with a low apparent bulk density, which means that in order to reduce the friction between particles bulk density should be high.

Hausner ratio: The ratio of the tapped density to the apparent density is known as the Hausner ratio (HR), which is expressed in equation 2.1. It is a special number to examine the powder flow regarding its density. It is commonly considered that if the ratio is greater than 1.25 it stands for poor flowability [13]. The Hausner ratio decreases with the reduction of the finer particles [17]. However with decreasing PSD Hausner ratio increases, causing poor flowability [18]. Also, the Hausner coefficient rises with a reduction in sphericity [19].

$$H = \frac{\rho_T}{\rho_A} \tag{2.1}$$

Carr Index: Another commonly used numerical value that indicates the flowability rate is the Carr Index (CI). It is generally assumed that if the index is greater than 20, it indicates poor flowability. Carr index also can be calculated using the tapped and apparent density of the powder and can be expressed as follows:

$$CI = (1 - \frac{\rho_T}{\rho_A}) * 100 \tag{2.2}$$

Table 2.2: Classification of powder flowability, using the Hausner ratio and Carr index

Flow behaviour	Hausner ratio	Carr Index
Excellent	1.00-1.11	0-10
Good	1.12-1.18	10-15
Fair	1.19-1.25	16-20
Passable	1.26-1.34	21-25
Poor	1.35-1.45	26-31

2.3 Tensile properties

316L stainless steel is one of the most preferred stainless steels due to its excellent mechanical properties, corrosion resistance, and bio-compatibility with the human body. SLM-printed 316L alloys have a distinctly different microstructure than their conventionally fabricated counterparts [20]. From the results of the study, it appears that the mechanical properties of SLM-printed stainless steel parts are highly dependent on changes in the microstructure. Therefore, studying the influence of build orientation and printing parameters is essential to further optimize these characteristics in order to obtain parts with both good strength and ductility.

According to most studies, 316L stainless steel fabricated by SLM has better mechanical properties regardless of the build orientation and heat treatment process. However, since the cooling rate in SLM is high, it can lead to significant residual stresses, which in turn can cause defects in the printed samples. Therefore, it is important to determine how heat treatment helps to overcome this problem. According to the literature, heat treated specimens have slightly lower tensile strength (UTS) and yield strength (σ_Y) than non heat treated parts, but the elongation after heat treatment is significantly higher. In most cases, previous studies have considered the correlation between build orientation and tensile properties or the effect of heat treatment on tensile properties, but not both parameters simultaneously. That is why this work aims to address this research gap by trying to correlate the effect of both build angle parameters and heat treatment process on mechanical properties. Table 2.3 summarizes the results of some studies on the mechanical properties of SLM-fabricated 316L stainless steel.

2.4 Fatigue

Fatigue properties depend on so many factors. Among them, studies on additively manufactured parts usually consider build orientation, surface processing, heat treatment, and presence of defects to affect fatigue performance significantly. It was found that while many studies were published on fatigue, they are difficult to compare due to repeatability issues inherent to 3D printing, because of residual stresses stemming from high cooling rates. Studies differ when considering the type of fatigue, namely high or low cycle, fully reversed or pulsating cycles, the number of axes where stress is applied, and et cetera. Thus, a research gap exists, which will be addressed in this study. This work is thus beneficial, since it has the advantage of having the same processing conditions, while encapsulating build orientation in a wide variety, as well as heat treatment. Surface processing was determined not to be as relevant as the other factors.

In general, it was found that fatigue behaviour of additively manufactured stainless steel is worse than that of their conventionally produced counterparts due to defects and presence of pores. In terms of surface processing, some studies reported a positive influence on fatigue performance. As for build orientation, flat printed (XY) samples were found to perform best. Regarding the effect of heat treatment, annealing with holding temperatures in the range of 900 to 1090 degrees Celsius were found to have a positive effect, especially on high cycle fatigue. Despite relatively definitive results, main limitations of all the studies were differing processing conditions, loading methods, and significant scatter of data. The summary of the literature review is displayed on Table 2.4.

Table 2.3: Literature review on tensile properties of SS 316L

Experimental conditions	**Material used**	**Result**	**Limitation**
Tensile specimens were fabricated with 90°, 75°, 60°, 45°, 30°, 15° and 0° to the building direction (z-axis). Quasi-static tension tests were performed in a Shimadzu AG-X universal test machine. Three tests were performed for each group of specimens.	Specimens were processed in a LPBF AM using gas-atomized stainless steel 316L powder with an average size of 50 μm [20].	The specimens with 90° and 75° inclinations exhibited the highest yield and tensile strengths, while the specimen with 0° inclination showed the highest fracture strain.	Assymetry in the tension and compression stresses caused by the residual stresses
The tensile tests were carried out by an Instron model 3366 at a nominal strain rate of 0.12 mm/min. Some specimens were heat treated at 1070°C for 1 h and then cooled down in air.	Three stainless steel 316L samples were compared: Conventional Manufactured, Powder Bed Fusion (PBF) and Direct Energy Deposition (DED) [21].	The AM 316L specimens prepared in this work had higher yield strength and tensile strength and lower elongation at failure than traditionally machined specimens. Heat treated specimens generated the lower yield and tensile strengths but the larger fracture elongations.	For some parts, post-processing such as polishing was applied, which may have affected the results.
ASTM E8 was used on the specimens used for mechanical testing. Mechanical tests were performed on a Zwick/Roell Z250 uniform testing machine. Specimens were printed vertically (90°) and horizontally (0°). The laser power was also varied.	316L stainless steel powder was used for SLM, the powder particle size was 20-53 μm [22].	Increasing the laser power increases UTS, σ_Y and elongation values. Horizontally build samples generated better mechanical properties than vertically build specimens.	There was no detailed discussion of the effect of laser power on microstructure and mechanical properties.

Table 2.4: Literature review on fatigue properties of SS 316L

Experimental conditions	**Material used**	**Result**	**Limitation**
Surface processing involves the following: as-built, shot-peened, and machined. Fatigue tests were carried out at room temperature using an MTS 858 fatigue machine. Fixed stress ratio of 0.1 with a 20 Hz sinusoidal loading were applied at every test with a cut off cycle of 1 billion.	A Renishaw AM 250 SLM was used to manufacture all SS 316L test samples. Virgin powder was used with a particle size in the range of 15 and 45 microns [23]. Short-peening was achieved using fine glass particles with a mean diameter of 250 microns at a pressure of 4 bar.. Machining was performed via turning from a solid rod.	Machined test samples showed a considerable increase in fatigue strength, compared to as-built samples due to a presence of surface defects and lack of fusion defects. Short-peened samples showed an increase in fatigue strength of 20 to 45 percent in high cycle fatigue region.	As suggested by the researchers, further study needs to be conducted in an even higher fatigue cycle range. Moreover, as Avanzini et al pointed out research into the effects of surface finish often has significant scatter throughout a multitude of studies, because fatigue properties are highly process dependent [24].
Characterization of the effect of build orientation on the fatigue strength of 3D printed samples. Cylindrical test samples were printed in horizontal (XY) and vertical (Z) orientations. FERITSCOPE MP 30E device was used to perform fatigue tests.	EOS M 290 SLM printer was used to manufacture all SS 316L test samples. Virgin powder was used with a powder particle size ranges between 25 and 45 microns [25]. Fatigue tests were conducted using load increase tests.	Horizontal test samples showed the highest fatigue performance. Fatigue behaviour of specimens was determined to depend on elongation of grains and the arrangement of boundaries of melt pools, both of which depend on the build orientation.	Further tests needed to be done at different angles, such as diagonal, to better understand how micro-structure depends on build orientation. Avanzini et al found that diagonal specimens often perform similar to flat printed samples [24].
Heat treatment is achieved by the following: Stress Relief, Annealing, and Hot Isostatic Pressing. Stress Relief involves temperatures in the range of 350 to 650 degrees Celsius in the duration of 1 to 9 hours.	Annealing involves temperatures usually in the range of 900 to 1090 degrees Celsius and a duration from 10 minutes to 2 hours. HIP is conducted at 1150 to 1190 degrees Celsius with applied pressures of 1000 to 1450 bars.	SR was found not to have significant effect on fatigue. Annealing was reported to have a positive influence, especially for high cycle fatigue. HIP was concluded to not have much of an influence as well [24].	Studies differ by processing conditions, which is why a comparison needs to be done within a single study. Additionally, it was reported that literature is lacking for annealing and HIP with only one paper reported within the review [24].

2.5 Hardness

Another major mechanical property of printed specimens is hardness, and the influence of different build angles and laser power on the performance of hardness is studied. Generally, grain refinement and dislocation have a great impact on hardness, therefore, optimization of the process parameters during SLM printing is considered a crucial factor, and some recent studies are presented in Table 2.5.

However, there exists a concern about the effect of heat treatment on the hardness of SLM-printed stainless steel. While prior studies have investigated the impact of build orientation on hardness, limited research has been conducted on how post-printing heat treatment affects hardness properties and there are differences in the data by build orientation. Understanding how heat treatment influences hardness is essential for assessing the overall mechanical behavior and performance of SLM-printed stainless steel. Therefore, investigating hardness before and after heat treatment fills this gap and provides valuable results into the optimization of post-processing treatments for enhancing material properties.

2.6 Corrosion

The corrosion properties of specimens fabricated using additive methods were investigated in different studies, and subjected to open circuit potential (OCP) and potentiodynamic polarization (PP) tests. Notably, in the OCP plot of Laser Powder Bed Fusion (LPBF) samples, there was an observed increase in potential alongside a constant current density. Moreover, as hatch spacing increased, the pitting corrosion of the samples exhibited a rise in potential, mostly attributed to porosity. This porosity facilitates crack propagation in corrosive environments, consequently leading to the development of pitting, and other parameter effects can be seen in Table 2.6.

According to several studies, the corrosion resistance of additively prepared specimens is affected by the dislocation subgrain structure, which contributes to enhanced pitting corrosion resistance and reduced crack development rates compared to conventional ways in a 3.5 wt% NaCl solution. Additionally, the concentration of NaCl solution affects the passive film on stainless steel; however, there is a limited study on deeper understanding of the corrosion behavior of SLM-printed stainless steel components, particularly concerning the influence of heat treatment on corrosion resistance; therefore this capstone project aims to assess how heat treatment impacts corrosion resistance, considering the unique microstructural characteristics of SLM-printed materials, which is essential for their practical application in various industries.

Table 2.5: Literature review on hardness properties of SS 316L

Experimental conditions	**Material used**	**Result**	**Limitation**
There are five different construction angles: 0°, 15°, 45°, 75° and 90°. The process parameters are defined as 675 mm/s of laser speed and 0.1 mm of hatch distance.	316L stainless steel prepared by selective laser melting [26].	The hardness indentation was the highest taken in the cross-section of specimens produced using parameters P=80 W and v=400 mm/s. After laser polishing, there is no effect on the surface microhardness of the as-printed material as there is no evidence of surface hardening.	Lack of correlation between specific laser polishing parameters used and changes in hardness measurement.
The samples were annealed at different temperatures up to 800ºC for 1 hour and then water quenched. The measurement was taken at a dwell time of 10 seconds.	LPBF 316L Stainless Steel [27].	The average microhardness value of the specimen was 252 HV. An increase in annealing temperature led to a rise to 291 HV up to 400°C, followed by a gradual decline to 228 HV.	There are variations in heat treatment conditions that can lead to inconsistent results.
Specimens are placed on the building platform at 0°, 45°, and 90° and heat treated at 650°C, 950°C, and 1100°C for 2 hours and are furnace cooled.	316L Stainless Steel [28].	Heat treatment results in a reduction in the hardness values of the 316L stainless steel. The smallest increase in hardness value was observed at the highest heat treatment temperature tested for 1100°C with a holding time of 2 hours.	There is a lack of comprehensive explanation of the effects of heat treatment on SLM 316L stainless steel and the factors that influence the final properties of the material.

Table 2.6: Literature review on corrosion properties of SS 316L

Experimental conditions	**Material used**	**Result**	**Limitation**
The specimens were printed horizontally, vertically, and 45° and immersed in 0.6M NaCl solution. Open circuit potential for 30 min and cyclic polarization testing at 1ms/V were performed.	316L stainless steel prepared by selective laser melting [29].	Horizontal specimen displayed the highest average corrosion potential followed by the 45° and vertical. There is no effect of porosity on pit initiation for SLM 316L SS.	Lack of investigation of the effect of porosity on increasing the susceptibility to pitting for higher concentration.
The electrochemical polarization was performed in a glass cell with a reference electrode of AgCl and a counter electrode of platinum wire under 0.1M NaCl solution.	LPBF 316L Stainless Steel [30]	LPBF 316L exhibited increased anodic current density in comparison to wrought 316L, and the reason behind that is heterogeneous solute distribution during printing.	Insufficient understanding of the mechanism of microstructural variables and passivity on LPBF 316L.
Open circuit potential, impedance test, and CPP were measured polarization of AM 316L with saturated calomel electrode and platinum sheet. All measurements were performed in 3.5%wt NaCl solution.	AM 316L Stainless Steel [31]	AM 316L exhibited reduced current density and increased corrosion potential in comparison with wrought 316L, where sub-grains corroded.	Insufficient understanding of the mechanism of microstructural variables and passivity on LPBF 316L.

Chapter 3: Methodology

3.1 Powder preparation and rheological characteristics

The first phase of the study is to analyze the powder characteristics, since the powder quality determines the properties of the final part. One of the key properties of powder is its flowability, which in turn can be evaluated by many factors such as density, PSD, particle morphology and powder manufacturing process. To properly evaluate the powder, the following experiments were conducted on the stainless steel powder from two different suppliers.

3.1.1 Materials

Two types of powder were utilized for SLM printing. The first powder was prepared by PREP and will be referred to as S1. Suppliers of the powder S1 state that PSD for powder is 15-45 μm. The second powder was gas atomized and will be further referred to as S2. According to specifications, the PSD for powder is 20-45 μm. Rheological properties for both of them were obtained in order to compare results with the literature review and assess the flowability of powders.

3.1.2 Rheological properties of powders

The rheological measurements were conducted by FT4 Powder rheometer. The FT4 Powder Rheometer is designed to more accurately assess the rheological behavior of powders due to its higher sensitivity[32]. The main properties for the study were dynamic flow, shear cell, and aeration. All tests were run three times to ensure consistency and reliability of results.

1. Dynamic flow testing is determined by applying normal force while the blade moves downward through powder to get precise flowability parameters. During the process, powder particles have induced interaction and movement. The resistance encountered by the blade represents the bulk properties. Basic flowability assessment gauges the dynamic flow of powder in a conditioned state, reflecting physical properties and moisture content.

2. The shear cell process involves calculating shear strength and cohesion properties. The powder is pre-consolidated to 10 kPa, and this force is applied to an upper layer of powder at very low speeds, inhibiting adjacent lower layers from moving. Until the force increases without any movement at the shear plane, the powder bed "yields," allowing the top layer of powder to slide across the bottom.

3. In the aeration process, air is introduced during the movement of blades, indicating the cohesive strength of the powder. Particle contact decreases and flow is produced with less energy when the powder is aerated. It also measures the aeration ratio (AR), which describes this reduction in flow energy.

3.1.3 Particle Size Distribution (PSD) and Morphology

PSD for both powders was determined using a Mastersizer 3000 instrument. The core of the equipment is the optical unit, and the process is that red laser light and blue light are passed through the samples and detectors can generate data on the samples using the light scattering pattern caused by the particles. All acquired data are interpreted in Mastersizer 3000 software.

The morphology of the samples was analyzed with a scanning electron microscope (SEM) ZEISS Crossbeam 540. This microscope allows to obtain high-quality nanofabrication and nanotomography of different samples. For both samples SEM images with magnifications of 200 X, 300 X, 500 X and 2000 X at 5.0 kV were taken to analyze the morhpology of powders .

3.1.4 Density of powders

The apparent bulk density of the powder can be characterized by its two types: apparent (aerated) bulk density and tapped bulk density. Apparent bulk density is determined using the Hall flow meter. A certain amount of powder is allowed to loosely flow through the Hall flow meter funnel and collected in a specified density cup (with a volume of 25 cm^3). After that mass of powder per unit of volume is taken as the bulk density of the powder.

Another type of density is tapped density, which is also random dense packing, and it determines the improved particle distribution by tapping the apparent bulk density. Tapping is a process that rearranges the powder particles in a more efficient manner, so the empty spaces between particles are filled. For the measurement of the tapped density Tap Density Meter DY-100A equipment was used. The procedure was conducted according to the international standard ASTM B527 Standard Test Method for Determination of Tap Density of Metallic Powders and Compounds. After getting the data of the apparent bulk density, the same powder is used to get the value of tapped density by tapping it 1000 times. Then mass of powder after tapping per unit of volume is taken as a tapped density of the powder.

Both density values play an important role in classifying the flowability of the powder. For consistency and accuracy, each procedure was performed three times and then the average values were calculated. All data are summarized in a table and presented in Table 4.4.

3.1.5 Chemical composition

The chemical composition of the powders was investigated by scanning electron microscope JEOL JSM-IT200 (LA). The small amount of powder was spread on carbon tape and placed in the chamber. The electron microscope uses a resolution of 3 nm at an accelerating voltage voltage of 30 kV. The analysis of chemical composition is provided in Table 4.2.

3.2 SLM printing

The samples of stainless steel 316L were processed by selective laser melting process by Renishaw AM 400. The processing parameters are identified as follows:

-Laser power: 200 W

-Hatch spacing and point distance: as recommended by the manufacturer

-Layer thickness: 50 μm

-Platform temperature: 170° Celsius

The samples are printed at 0°, 45°, 55°, 65°, 75°, 85°, and 90° angles of orientation and the dimensions of each test are different in accordance with ASTM standards.

3.3 Mechanical properties of the printed parts

After the parts are printed, several tests are performed to evaluate the mechanical properties of the SLM-printed samples. These tests include:

1. Tensile test to evaluate strength and toughness of the SLM printed parts
2. Fatigue test to evaluate the strength of printed parts under repeated loading
3. Hardness test to investigate the resistance of stainless steel to plastic deformation
4. Corrosion test to investigate the corrosion behaviour of the printed parts

Each of the tests was performed on samples with different build direction to investigate how the mechanical performance of printed parts can be optimized using variable SLM parameters.

3.3.1 Heat treatment

All tests were performed with and without heat treatment as a post-processing step to evaluate the effect of heat treatment on the mechanical properties and corrosion of the material. The specimens were heat treated at 1000° Celsius for 30 minutes and then cooled

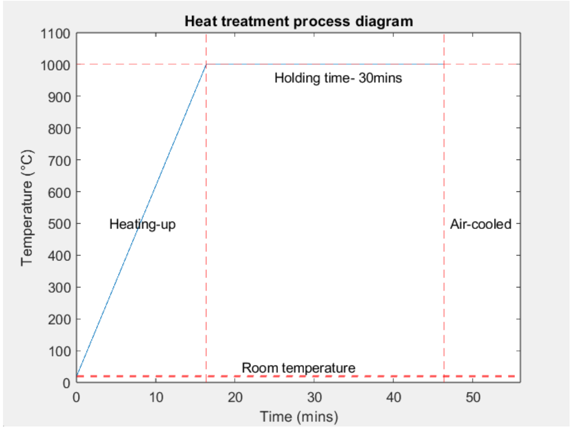

Figure 3.1: Heat treatment process diagram

in air. SNOL Muffle Furnace with E5CC-T Controller was used for the process. The heat treatment process is illustrated in Figure 3.1.

3.3.2 Tensile test

To conduct standard tensile tests, a CMT electronic universal testing machine was used (Figure 3.2a). The test is low-strain (static) with a speed of 3 mm/min. The geometry of the tensile testing samples was chosen from the ASTM E8M standard (Figure3.2b). The gauge length (30mm) was five times the gauge diameter (6mm). The specimen is subjected to a tensile loading which will increase the stress in the gauge section until it has achieved its maximum ultimate tensile strength (UTS). The machine also provides information on the deformation of the specimen throughout the test. A computer connected to the machine produces a stress-strain curve and records all loads, stresses and displacements. From all the data obtained, properties such as YS, UTS, toughness and elongation can be estimated which will be further used to study the strength and ductility of the material. For consistency, samples for each angle were tested at least two times and average values were calculated.

3.3.3 Fatigue test

To perform fatigue tests, a HST-P50 Electro-hydraulic Servo Dynamic static fatigue testing system was employed (Figure 3.4a). The geometry of the specimen is depicted in the Figure 3.4b. HST-P50 conducts two types of tests: load (stress-based) and strain (strain-based). For all the specimens, stress-based fatigue tests were conducted with axial loading mode, where upon fixation of the cylindrical specimen from both sides, one grip is fixed, while the second oscillates in a sinusoidal wave-like manner. Sinusoidal wave loading is depicted on Figure 3.5 along with the relevant load parameters. Among which, most important are the following: stress amplitude, maximum and minimum stresses, fatigue

(a) (b)

Figure 3.2: Tensile testing (a) CMT Electronic Universal Testing Machine, (b) Drawing of the tensile test specimen- ASTM E8. Dimensions are in mm

load ratio (R), and equivalent stress, using the Smith-Watson-Topper (SWT) correction. All tests underwent an alternating load ratio (R=-1), where mean stress is zero. Amplitude stress was chosen to be a portion of the yield stress, so that seven stress points were tested: 90, 80, 70, 60, 50, 40, and 35 percent of the yield stress. A fatigue specimen printed at a 45 degree angle underwent tensile testing to set a benchmark yield stress for the rest of the specimens. As a result, 580 MPa was taken to be a benchmark yield stress for fatigue testing. As for the equivalent stress, a Smith-Watson-Topper correction was chosen due to its wide popularity for purposes of comparing fatigue results of different studies. Thus, for comparison of results with those of other studies, all stress loads will be converted using the following SWT correction:

$$\sigma_{ar} = \sigma_{max} * \sqrt{\frac{1-R}{2}} \tag{3.1}$$

To characterize fatigue strength, S-N curves were plotted, using the data obtained from the HST-P50 static fatigue testing machine. As it was previously mentioned, an alternating load was applied, where the load ratio was equal to -1, meaning that mean stress was zero for every test. After the tests, fracture surface was analyzed through the use of SEM imaging, where clear differences in the morphology of heat treated and non heat treated samples can be noticed. Before testing, to determine the load levels, a fatigue specimen printed at 45° underwent a tensile test to determine yield stress. As a result of which, amplitude of alternating stress was determined as a fraction of the yield. It was found in the literature that 40% of yield stress is expected to be the endurance limit for 316L stainless steel.

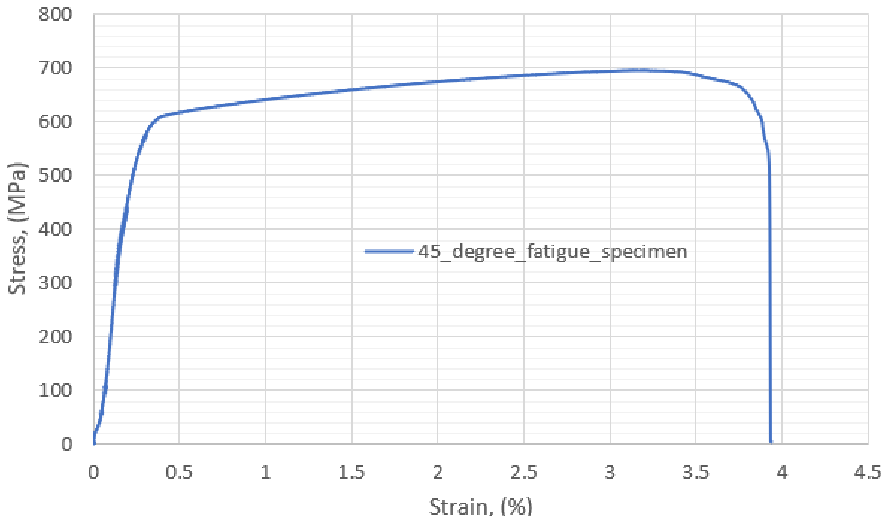

Figure 3.3: Stress-strain curve for a 45° SLM printed specimen without heat treatment

Stress-strain curve of the 45° specimen is depicted in the Figure 3.3. From the figure, yield stress was determined to be at around 580 MPa and ultimate tensile stress at 700 MPa. The literature review suggested to use loads corresponding to the fractions of the yield stress. Moreover, to get an accurate comparison of fatigue strength of different specimens, the same stress loads were used for all build orientations. Apart from that, to make it easier to compare the results of this study to those found in the literature, Smith-Watson-Topper (SWT) correction was used, using the Equation 3.1. Table 3.1 depicts the amplitude of stresses applied to characterize fatigue performance.

Table 3.1: Stress loadings for fatigue test

% of σ_{Yield}	90	80	70	60	50	40	35
$\sigma_{Amplitude}$ (MPa)	517	462	398	350	279	239	199
σ_{Ar} (MPa) per SWT	517	462	398	350	279	239	199
Load (N)	6500	5800	5000	4400	3500	3000	2500

3.3.4 Hardness test

The evaluation of hardness was performed by micro Vickers hardness tester (Shimadzu HMV-G Series). The experiment was made under a maximum force of 1.96 N (200 gf) at a holding time of 15 s. The specimen has a size of 20x20x5 mm and is polished with sandpaper to determine the desired area's hardness. The distribution of indentations in the shape of a small diamond pyramid spaced 0.4 mm apart, with the average value of more than 10 indentations representing the hardness. Its representation can be seen in Figure 3.6.

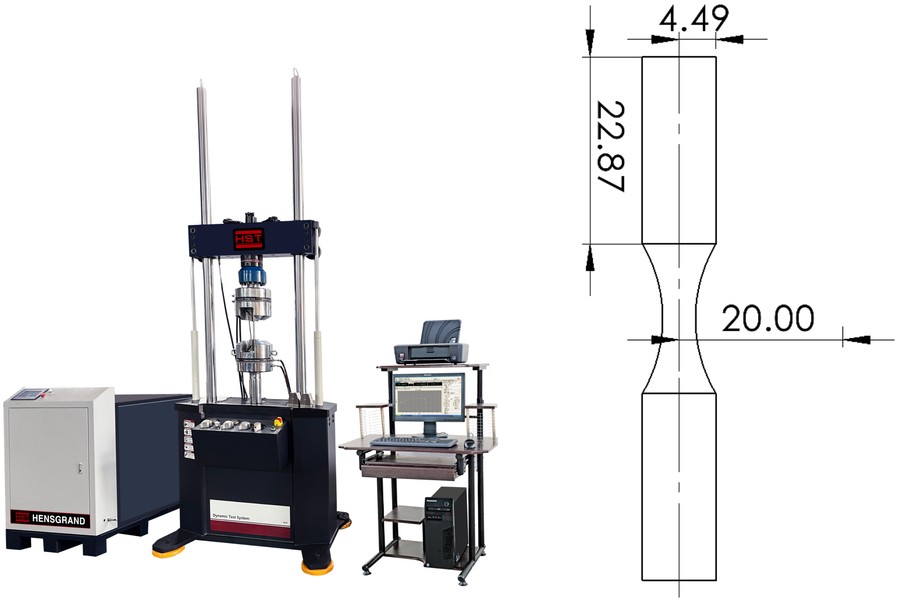

(a) (b)

Figure 3.4: Fatigue testing (a) HST-P50 static fatigue testing system, (b) Drawing of the fatigue test specimen. Dimensions are in mm

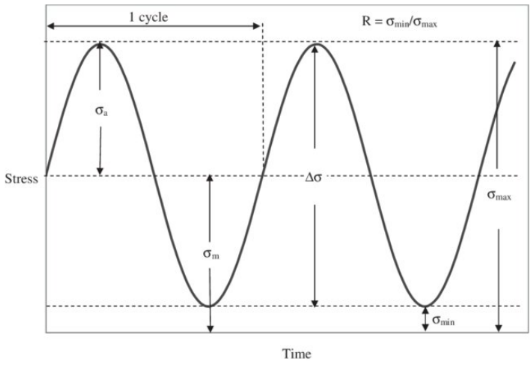

Figure 3.5: Description of sinusoidal loading [1]

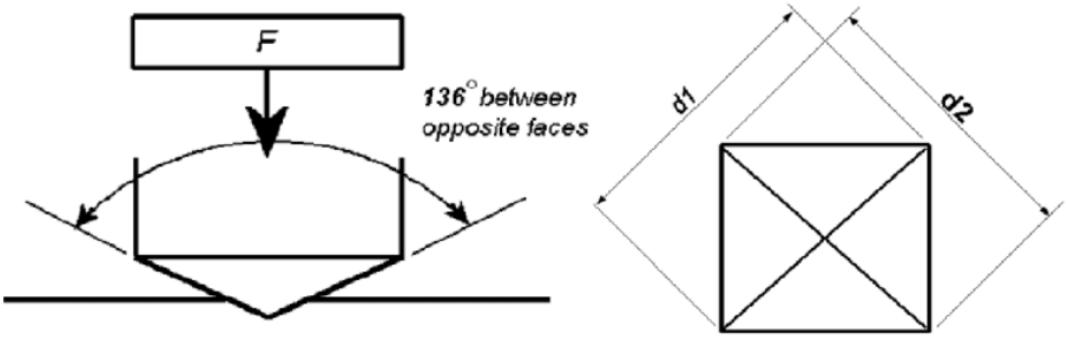

Figure 3.6: Illustration of Vickers hardness test

3.3.5 Corrosion

The corrosion testing was performed using Corrtest Potentiostat / Galvanostat 350 with SLM-printed 316L stainless steel. The reference electrode was silver chloride (AgCl) 3.5M. The counter electrode was platinum wire. The working electrode was the specimen sealed with epoxy resin with the circular exposed area (2.0 mm x 37 mm) and coated with plastic. The set up can be seen in Figure 3.8.

Tafel plot is the graph used for visualizing of corrosion rates by plotting the potential versus the logarithm of the current density. The straight line in Figure 3.7 gives gradients: anodic β_a and cathodic β_c. From the plot, corrosion current density and potential are determined by the intersection of points where the reduction reaction and oxidation reaction meets.

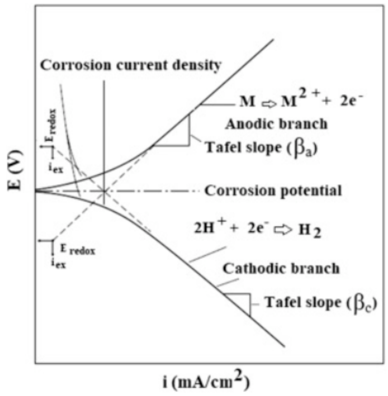

Figure 3.7: Illustration of Tafel curve [2]

The corrosion rate is calculated according to these slopes of Tafel curve (β_a and β_c), polarization resistance (R_p), and Stern-Geary equation:

$$i_{corr} = (\frac{\beta_a * \beta_c}{\beta_a + \beta_c}) * (\frac{1}{\mathbb{R}_p}) \tag{3.2}$$

$$i(mm/a) = i_c orr * 27.9 * \frac{393.7}{\rho} * 365 * 24 * 3600 * \frac{1}{39.37 * 96500} \tag{3.3}$$

As the electrodes are submerged in sodium chloride, the corrosion of stainless steel involves the following reactions:

$$Fe \rightarrow Fe^(2+) + 2e^-(anodic) \tag{3.4}$$

$$2AgCl + 2e^- \rightarrow 2Ag + 2Cl^-(cathodic) \tag{3.5}$$

$$2Cl^- + H_2O + 2e^- \rightarrow Cl_2 + 2OH^-(cathodic) \tag{3.6}$$

These equations assume the oxidation process of iron at working electrode and the reduction of silver chloride at the reference electrode. At the same time, chloride ions are reduced to form chlorine gas and hydroxide ions.

The tests were performed twice for each built direction, and then the microstructure of the samples was studied with a scanning electron microscope. The sample was placed in an electrochemical cell filled with 3.5 wt NaCl solution. This cell allows for controlled electrochemical reactions to take place on the metal surface. Before the test, the working electrode was exposed for 7200 seconds to stable open circuit potential (OCP). Electrochemical spectroscopy was performed by applying a 10 mV perturbation signal in a frequency range of 10 kHz to 10 mHz. The stable potentiodynamic experiment is executed at a scan rate of 5 mV/s in the potential range of -0.1 and 1 vs. OCP. The microstructure of the samples was studied with a scanning electron microscope. The results of the corrosion rate obtained by equations 3.2 and 3.3 are represented in Chapter 4.

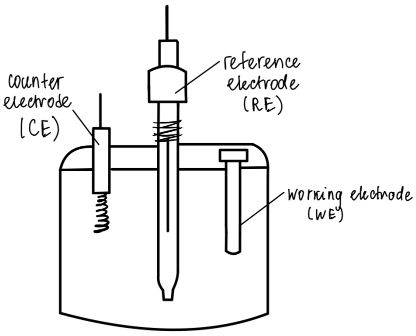

Figure 3.8: Corrosion test set up

Chapter 4: Results and Discussion

4.1 Rheological properties of the powder

Parts for the mechanical property tests were printed using the stainless steel powder obtained from two different suppliers. The difference in their rheological characteristics and their effect on the powder flowability were investigated. Rheological properties correspond to the behaviour of the atomized metal powder in response to an applied stress. On the other hand, flowability is a property of atomized metal powder that highlights its ability to flow. Flowability is crucial, since atomized powder will not lay uniformly on the printing platform, unless it is free-flowing. The lack of uniformity within a powder layer might result in less than 100 percent part density, which might lead to voids inside the printed parts that decrease the mechanical performance of 3D printed specimens.

4.1.1 Rheometer FT4 analysis

The results of three tests are obtained and represented in Figure 4.1. Shear testing experiments are employed to measure the flow properties of particles, including parameters such as the flow function, angle of internal friction, and bulk density. It represents shear resistance encountered by the blade during movement, implying that the downward force should correspond to the force acting on the blade. Notably, both powder samples, S1 and S2, exhibit nearly identical bulk density (BD), however, there is a difference in the values of the angle of internal friction for the powders, with averages of 16.4° for S1 and 23.1° for the S2.

Based on the previous study, for 316L stainless steel utilized in SLM printing, the powder comprises spherical particles and tends to have its effective internal friction angle of 28.6 ± 0.5° [33].

Another essential parameter for evaluating flowability is the flow function (FF), where values below 4 indicate poor flow and those above 10 suggest good flow. In the case of S1, the flow function is 33.5, and for S2, it is 26.1, indicating good flowability for both powders.

Moreover, Volume Flow Rate (VFR) test was conducted for powder flowability characterization. VFR quantifies total energy spent to move the blade without any significant resistance from the powder. Such energy spent is crucial, because it signifies the extent of how little energy is required to make powder particles free-flowing. The lower the value, the better the powder flowability. From the VFR analysis, it was concluded that total energy measurement spent on S1 powder was, on average, a 100 milliJoules less than that of S2 powder. As a result, it was concluded that VFR analysis verified the superiority of S1 powder for the purposes of additive manufacturing. However, it is notable that the difference in the values between the two powders was not significant enough to deem S2 powder unusable.

The last dynamic flow testing is aeration. During the aeration test, air at different velocities was induced into the powder, and the energy required to go through the powder was recorded. High required energy indicates that particles are cohesive since they are not separating well even with the inclusion of air. Comparing the results of the aeration test for powders from the Figure 4.1, it can be noticed that initially, powder from S1 requires significantly less energy in comparison with the powder from S2. This indicates that powder from S2 tends to agglomerate more, and these results are further justified with the PSD and SEM analysis.

4.1.2 Particle size distribution

The particle size distribution (PSD) of the powder was analyzed on a Mastersizer 3000. The data obtained using Mastersizer includes important parameters such as D90 (size less than 90 percent of the distribution), D50 (average particle size) and D10 (size less than 10 percent of the distribution). In addition, another important characteristic known as span is presented in the results. The span of the powder distribution has a significant effect on the flowability of the powder. The flowability of the powder improves when the span value decreases, and conversely, the flowability of the powder deteriorates when the span increases (Engeli, 2016). The span values for particles are calculated as follows:

$$Span = \frac{D_{90} - D_{10}}{D_{50}} \tag{4.1}$$

The results obtained with the Mastersizer 3000 are presented in the Table 4.1. Additionally, the PSDs of both atomized powders can be seen on Figure 4.2. The actual PSD is slightly higher than the values reported by the suppliers. The PSD of powder S2 is wider, indicating that there is more space between the particles, which increases the span. Regarding the magnitude of the span of the powders, since the PSD of powder S2 is wider, the span is also larger and is 0.684, while for powder S1, the span is 0.452. As mentioned above, a smaller span value indicates better flowability, since a narrower span is an indication of efficient particle packing and powder homogeneity.

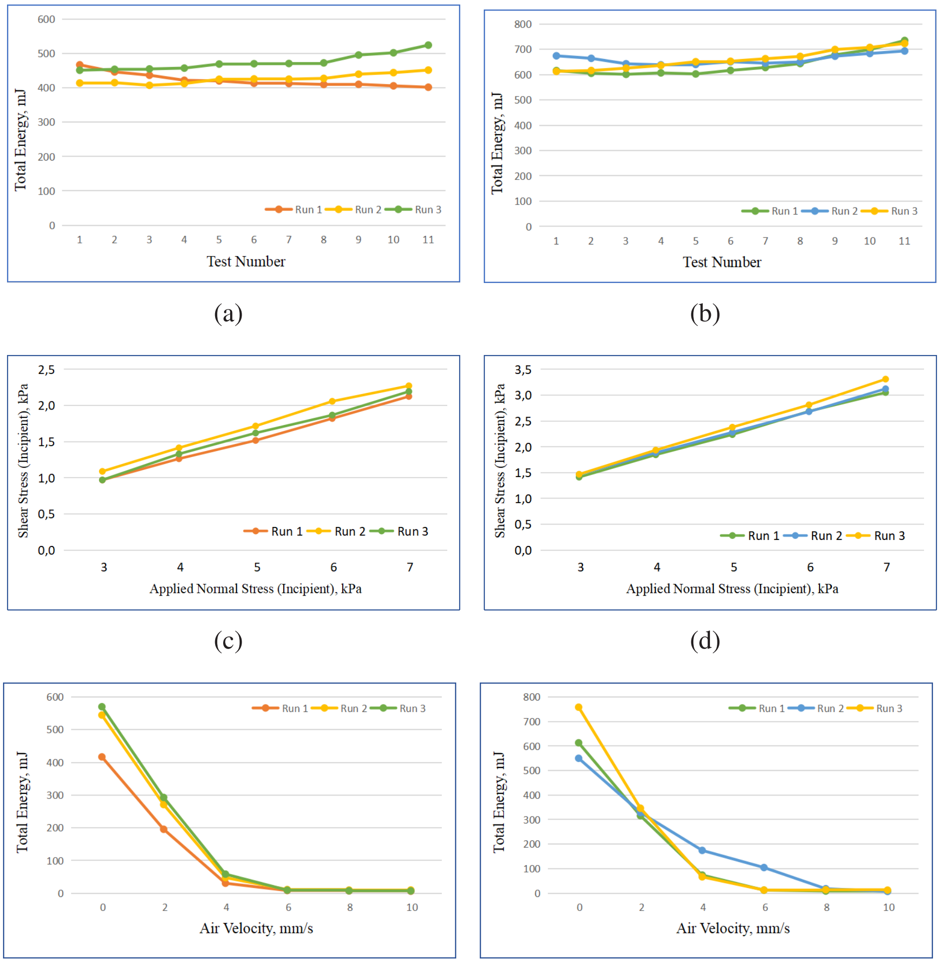

(a) (b)

(c) (d)

(e) (f)

Figure 4.1: Rheometer analysis for S1 and S2 (a) and (b) Basic flow energy, (c) and (d) Shear cell, (e) and (f) Aeration energy

4.1.3 Powder morphology

SEM images with magnifications of 200 X, 300 X and 500 X at 5.0 kV were taken to analyze the morhpology of powders. All images are presented in Figure 4.3 and Figure 4.4. From the images, it can be seen that powder S1 has more spherical and homogeneous particles, that is, the difference in particle size is not as large as for powder S2. Meanwhile, S2 powder particles have a more irregular shape and a large number of satellites on the surface. Satellites on the particles cause agglomeration, which indicates increased cohesion of the powder, and hence worsens its flowability. These observations are consistent with the results obtained from the rheological analysis, as the aeration test showed that the S2 powder particles are more cohesive. However, the reason that the powder S2 has a more irregular shape compared to S1 is because S1 was prepared by the PREP method, and this technique produces almost perfectly spherical particles. Whereas, the gas atomized powder has a less spherical shape due to a rougher powder preparation process involving atomization with a high pressure inert gas stream.

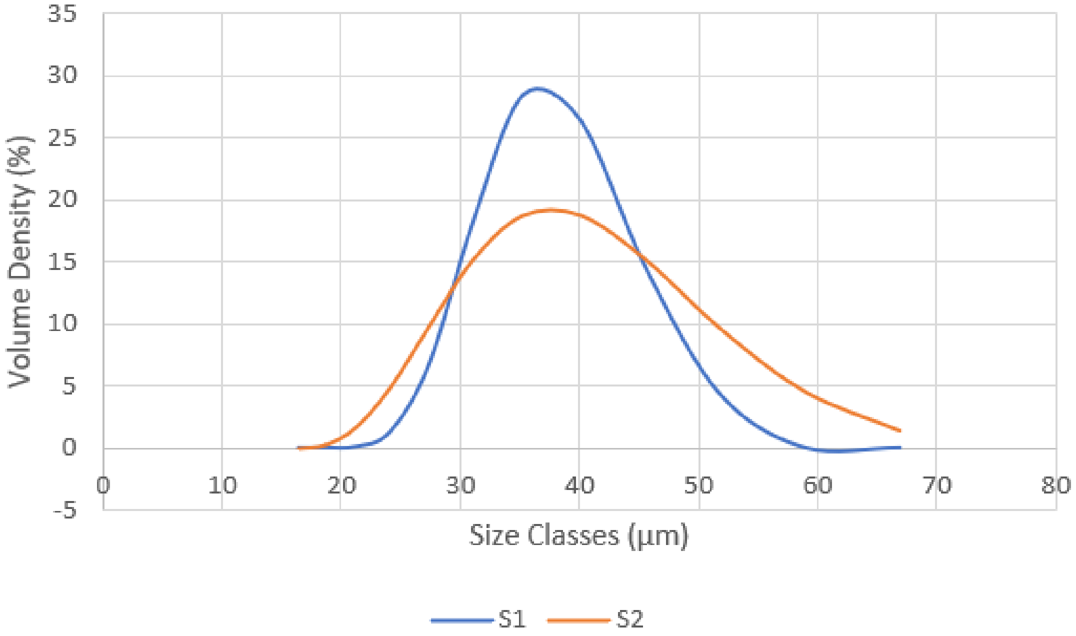

Figure 4.2: Particle size frequency distribution curve for both suppliers' atomized powders

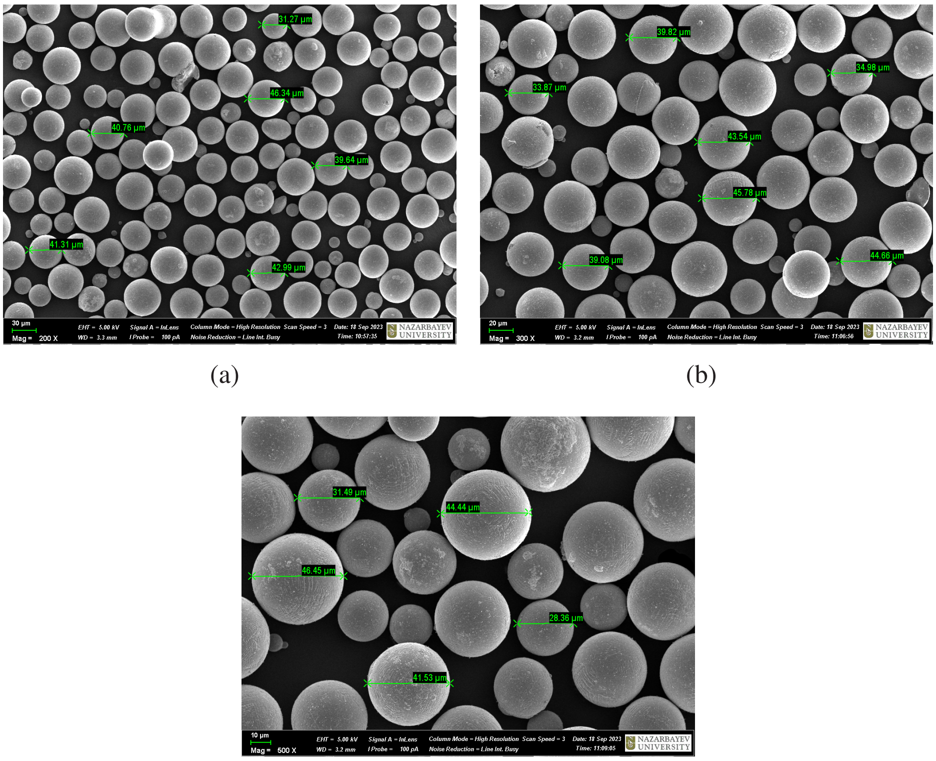

(a)

(b)

(c)

Figure 4.3: SEM images of powder S1 with different magnifications; a) 200 X, b) 300 X, c) 500 X

Table 4.1: Particle Size Distributions of both supplier powders

PSD parameter	**S1 powder**	**S2 powder**
Concentration:	0.0037 %	0.0050 %
Uniformity:	0.138	0.210
Specific Surface Area:	155.0 m^2/kg	155.1 m^2/kg
D[3,2]:	37.2 μm	38.2 μm
D[4,3]:	39.8 μm	41.2 μm
Span:	0.452	0.684
Result Units:	Volume	Volume
Dv(10):	31.5 μm	28.5 μm
Dv(50):	39.3 μm	40.0 μm
Dv(90):	49.3 μm	55.9 μm

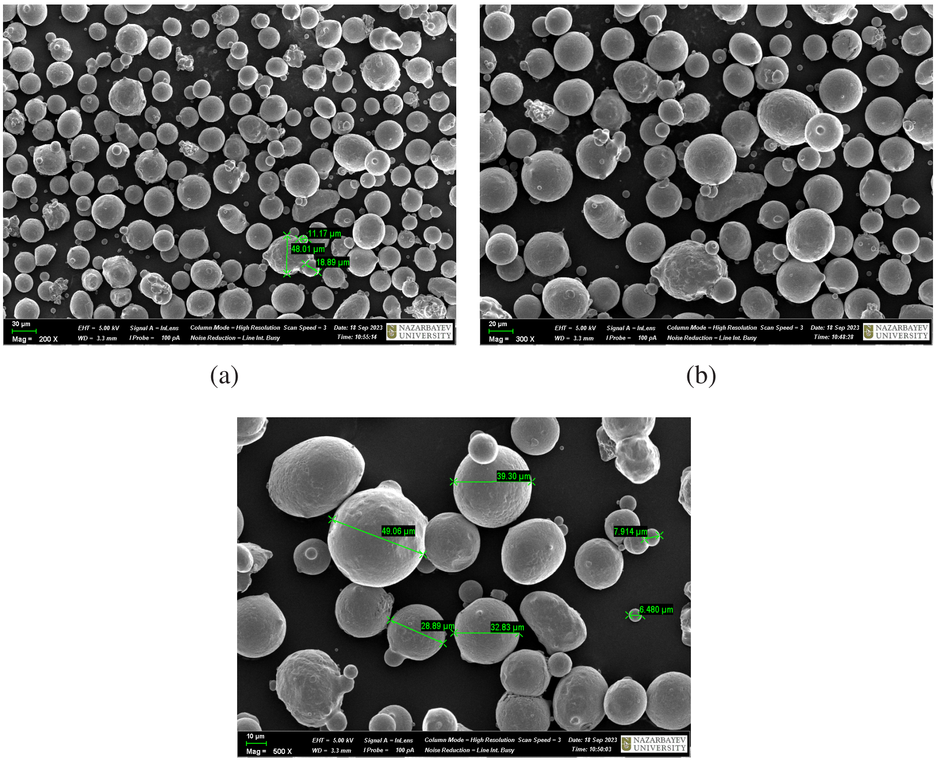

(a)

(b)

(c)

Figure 4.4: SEM images of powder S2 with different magnifications; a) 200 X, b) 300 X, c) 500 X

4.1.4 Chemical composition

The chemical composition was identified by scanning electron microscope, and it revealed that both powders were predominately composed of Cr and Ni. The concentration of molybdenum in both S1 and S2 is confirmed to be less than 2wt%, indicating that this element is intentionally incorporated to provide improved corrosion resistance. The concentration of oxygen in S1 and S2 reveals that the powders have undergone some degree of oxidation, with levels of 5% and 6%, respectively.

Table 4.2: Chemical composition of powder S1 and S2

wt%	**Al**	**Si**	**Cr**	**Mn**	**Ni**	**Mo**	**Fe**
S1	0.31	0.65	18.51	1.27	9.02	1.29	63.09
S2	0.34	1.08	18.67	1.94	10.32	1.38	59.70

4.1.5 Density of powder

Apparent bulk and tapped densities of powders are tabulated in Table 4.4. Density of the powder S1 is higher than the S2. However after tapping the change in the density is higher for the S2, meaning that bulk powder is not packed as efficiently and there was more empty spaces. The smaller the difference between tapped and bulk density of powder, the better the powder characteristics, since it means that powder particles are initially packed efficiently and has uniform distribution.

In addition, these two types of densities can be used to calculate numerical values known as the HR (equation 2.1) and the CI (equation 2.2), which are commonly used to evaluate powder flowability. As already noted, an HR greater than 1.25 is indicative of poor flowability, as it points out that the tapped density of the powder is significantly greater than the bulk density. Similar trends are observed for the CI, which is also a widely used numerical measure for powder characterization. The CI is calculated from the Hausner ratio, so a higher CI (usually greater than 20) indicates a moderate flowability of the powder.

Classification of powder flowability, using the Hausner ratio and Carr index are shown in Table 4.3. Based on the values obtained, both powders have excellent flowability according to the classification given in Table 2.2. However, when the powders are compared with each other, the HR and CI values indicate that the characteristics of S1 powder are a little better than S2 powder.

Table 4.3: Hausner ratio and Carr index of powder S1 and S2

	Hausner ratio	Carr Index
S1	1.017	1.683
S2	1.049	4.727

Table 4.4: Apparent bulk and tapped densities of powder S1 and S2

Apparent bulk density (g/cm^3)				
Powder / Run	1	2	3	Mean
S1	4.693	4.689	4.680	4.687
S2	4.361	4.377	4.388	4.375
Tapped density (g/cm^3)				
Powder / Run	1	2	3	Mean
S1	4.774	4.695	4.835	4.768
S2	4.655	4.523	4.598	4.592

4.2 Mechanical properties of printed parts

The outcomes of the mechanical properties testing are outlined below, offering valuable insights into the performance of components produced through SLM printing. The investigation included a thorough examination of the correlation between build direction and mechanical characteristics, uncovering significant observations. These findings contribute to an understanding of how the build orientation during the printing process influences the resulting mechanical properties.

4.2.1 Tensile testing

Mechanical properties of 316L stainless steel were evaluated using standard tensile tests. Based on these tests, it was possible to study the behavior of the material as a function of build orientation and heat treatment (HT) process. In this section, the build angles will be compared with each other for the following mechanical properties: Ultimate Tensile Strength (UTS), Yield Strength (σ_Y), elongation, toughness and elastic modulus. During the testing of the 55° (as build) and 85° (after HT) specimens, specimens slipped out of the tensile machine grips, which could cause inconsistencies in the data obtained. In addition, some samples failed prematurely, resulting in considerably low values. The results obtained for these samples are quite different from the specimens at other angles, so they should be considered statistically insignificant. However, the surface morphology of prematurely failed parts was studied in comparison with normal specimens. Stress-strain curves for specimens fabricated at different angles (as build and heat-treated) are shown in Appendix B (Figure B.1 (a), (b)).

1. Ultimate Tensile Strength (UTS)

According to results obtained from several tests (Figure 4.5), it can be noticed that UTS values of samples build at angles of 45°, 65°, 75° and 85° are in the range of 596-601 MPa. Meanwhile, for samples of 0°, 55° and 90° UTS values are relatively lower, 588 MPa, 560 MPa and 575 MPa respectively. For 0 degree, it is more or less expected to be lower than other samples, because of residual stresses left from supports while printing and due to high temperature gradient after printing [34]. Slightly lower values were also expected for the 90° specimens because load is applied normal to the printing direction. However, these results were not expected for the 55° specimens and this is an anomaly that appeared during the tests. This can be explained by the slippage during the tests mentioned earlier, so the results obtained for the 55° specimens should be considered with cautions and the tests need to be re-run.

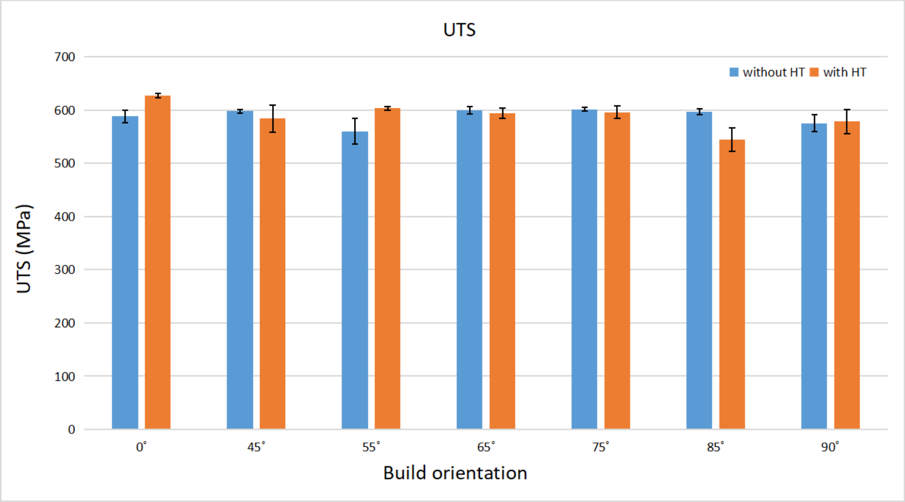

Figure 4.5: UTS vs. build orientation for specimens without HT and with HT

Generally, after heat treatment, the strength of the parts decreases slightly, affecting properties such as UTS and yield strength, while ductility increases significantly. After heat treatment, the UTS of the specimens at 0° increased significantly, reaching 627 MPa. This can be explained by the relieving of residual stresses, which improved the properties of the samples.The specimens at this angle are expected to withstand higher loads because load acts in the same direction as the printing. As for the other angles, samples build at angles of 45 and 95 found to have a lowest UTS values after heat treatment. For the 85° samples, UTS is 544 MPa, this is an unexpectedly low value, which may be due to same reason as for 55° samples, those results should be considered with cautions and tests should be redone.

2. Yield Strength (σ_Y)

Results of the yield strength are presented in Figure 4.6. The specimens fabricated at 90° and 85° angle showed the lowest values, about 430 MPa and 440 MPa respectively, while the yield strength at other angles ranged from 448 to 457 MPa. The lower yield strength of the specimens fabricated in the vertical direction is explained by the same reason as before: loading axis is perpendicular to the printing direction.

The inclusion of heat treatment showed that the yield strength of SLM fabricated parts is strongly influenced by changes in the microstructure caused by stress relief. Overall, yield strength of heat-treated specimens decreased significantly, and these results observed in other research works [34, 35, 36]. This is explained by the rearrangement of dislocation

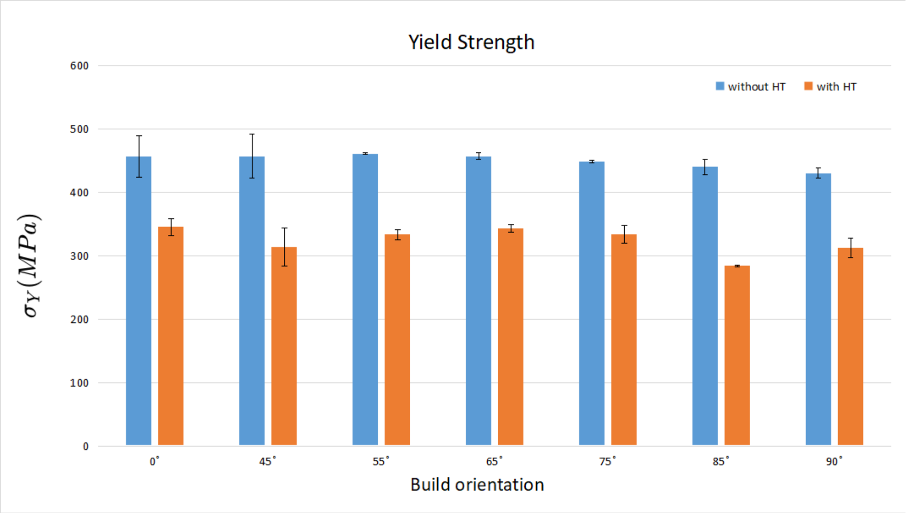

Figure 4.6: Yield strength vs. build orientation for specimens without HT and with HT

lines to reduce the energy, as grain sizes increase after heat treatment [34]. Specimens built at an angle of 0° have high value of yield strength.

3. Elongation

Elongation of SLM-fabricated parts also does not have any clear trend with the build orientation (Figure 4.7). Before heat treatment samples built at angle of 90° exhibited lowest elongation, while heat treated samples of the same angle elongated the most after heat treatment (Figure 4.10).

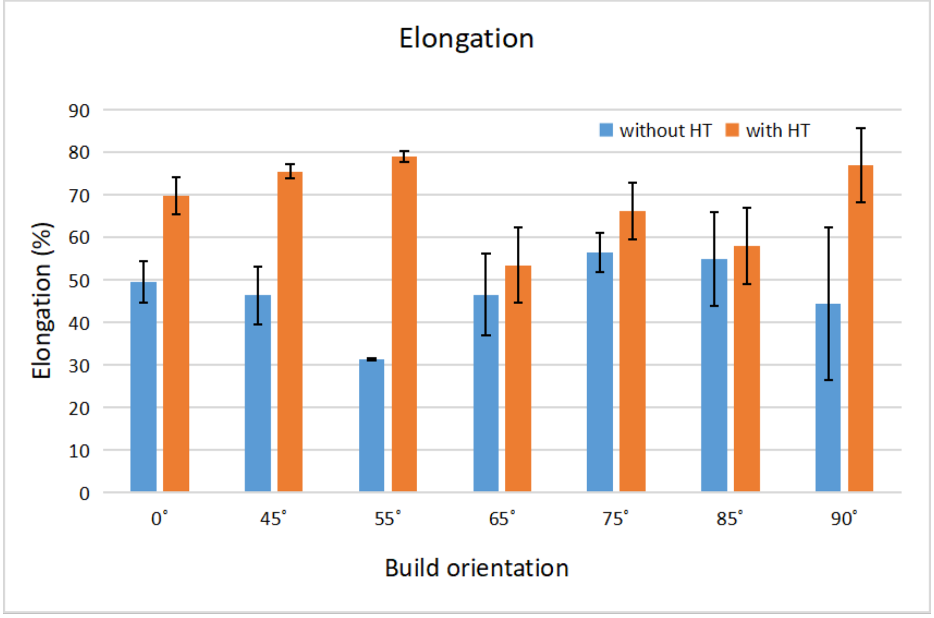

Figure 4.7: Elongation vs. build orientation for specimens without HT and with HT

After heat treatment, specimens became more ductile with a significant increase in elongation. Moreover, stress-strain curves (Appendix B.1 (b)) of the heat-treated specimens clearly show that necking occurred in most specimens before fracture, which is not the case for as-built specimens. These changes in mechanical properties, namely increase in ductility and decrease in strength, are primarily due to microstructure changes after heat treatment. The fracture surface morphology of as build and heat treated SLM fabricated specimens are shown in Figure 4.8. After heat treatment process, dislocation density and sub-grains were reduced, which resulted in improvement of ductility [37, 35]. It was observed that there was a relatively large number of pores and balls on the as build specimen's fracture surface in comparison to heat treated samples, which improved the elongation of parts. Heat treatment significantly reduces the number of pores and melts all the unmelted powder particles in the sample, and these defects are considered to be one of the main causes of premature failure [37].

4. Toughness

The toughness of specimens was calculated by finding the area under the stress-strain curve, and results for toughness corresponded to the results for elongation (Figure 4.9). This is because these two concepts are closely related, i.e. the more the parts were elongated, the more energy they absorbed. However, in general, toughness is also closely related to applied stresses. A high toughness does not always indicate a high ductility of the material. The most effective toughness is a balanced combination of high strength and ductility. In the case of this study, the toughness is more related to the change in elongation rather than to the stress values, since, according to previous results, differences in UTS values are insignificant.

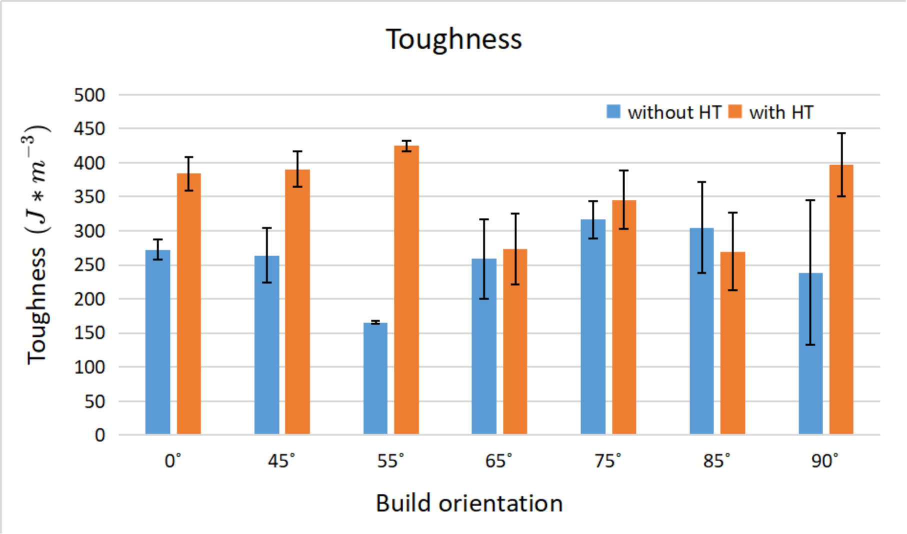

Figure 4.9: Toughness vs. build orientation for specimens without HT and with HT

All specimens absorbed more energy after heat treatment. Particularly significant increases can be seen for specimens fabricated at 0°, 45°, 55° and 90° angles, which had the lowest toughness values before stress relief. These results indicate that the combination of strength and elongation of the material becomes better after heat treatment, allowing much more energy to be absorbed.

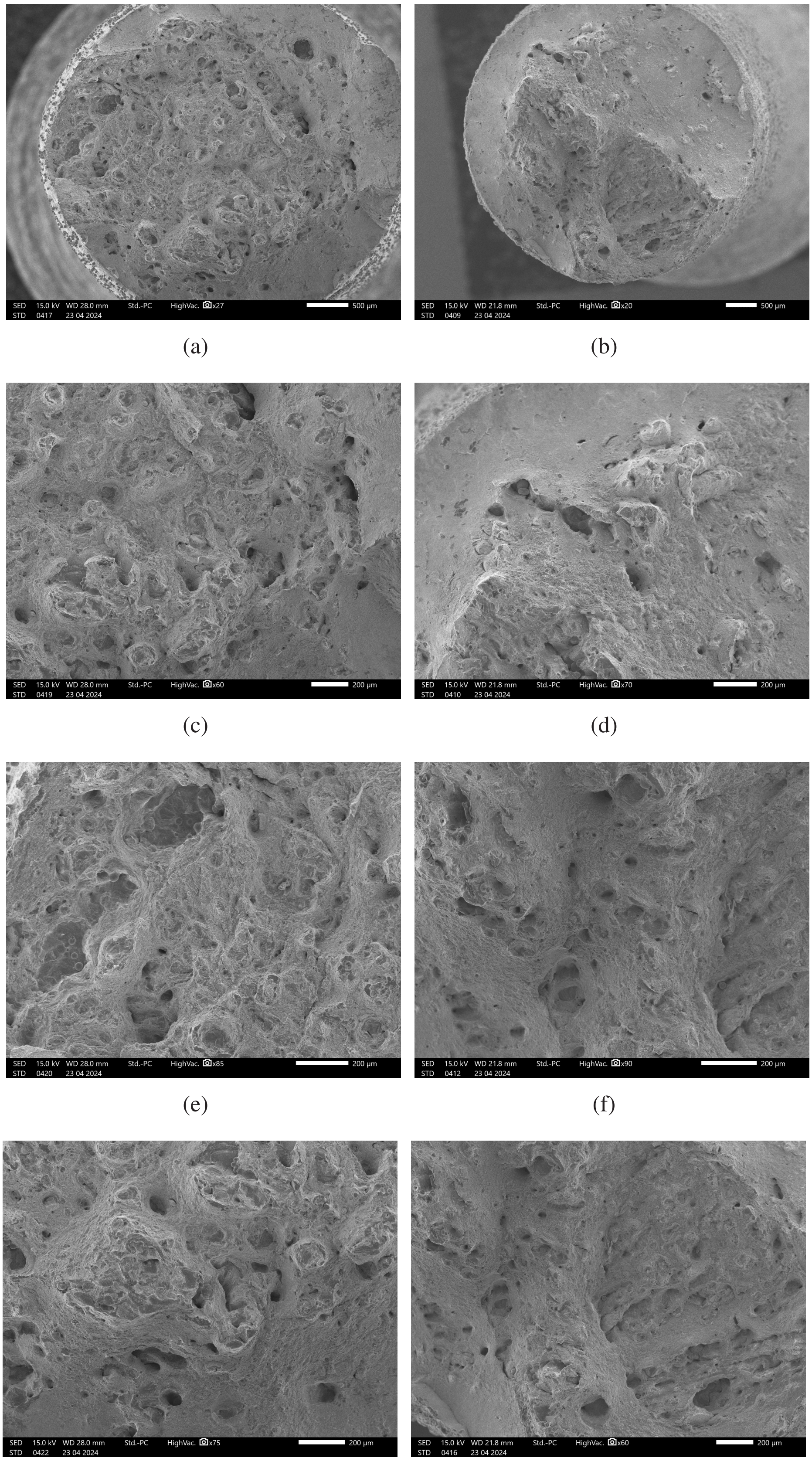

(a) (b)

(c) (d)

(e) (f)

(g) (h)

Figure 4.8: Fracture surface of 1) as build specimen fabricated at 90° (a) low magnification view, (c), (e) and (g) high magnification view and 2) heat treated specimen fabricated at 90° (b) low magnification view, (d), (f) and (h) high magnification view

(a) (b)

Figure 4.10: Tensile specimens with build orientation of 90° after fracture, (a) as built (b) as built and heat treated

5. Modulus of elasticity

Modulus of elasticity results has the highest standard deviation values (Figure 4.11), which may cause inconsistency in drawing conclusions and correlations between build orientation and heat treatment process. This may be due to the approximations made to find the best-fit value, as there was no clear linear function in the elastic region of the stress-strain curve. However, one trend is observed for samples with all angles of inclination: Young's modulus becomes higher after heat treatment. This result can be correlated with the reduction of the residual stresses after heat treatment.

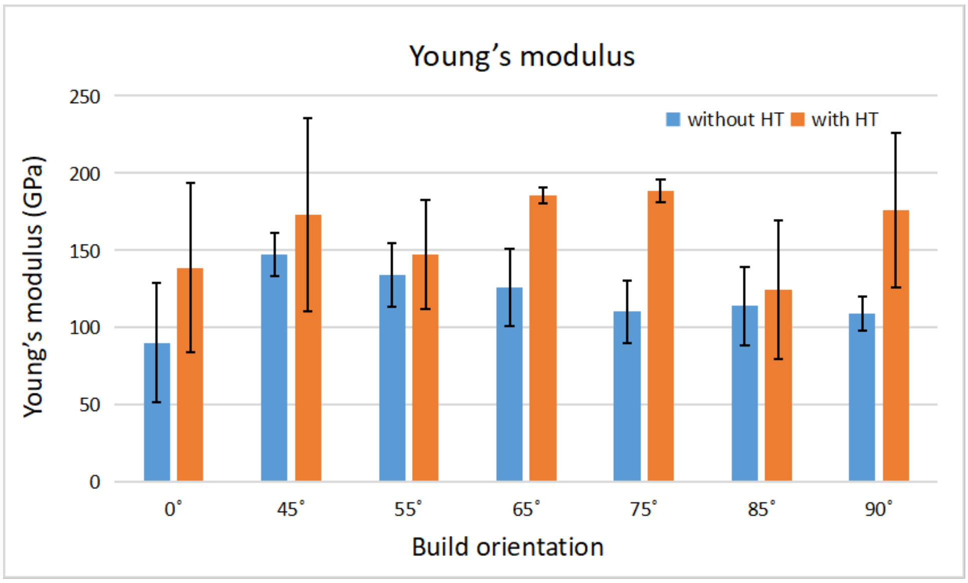

Figure 4.11: Young's modulus vs. build orientation for specimens without HT and with HT

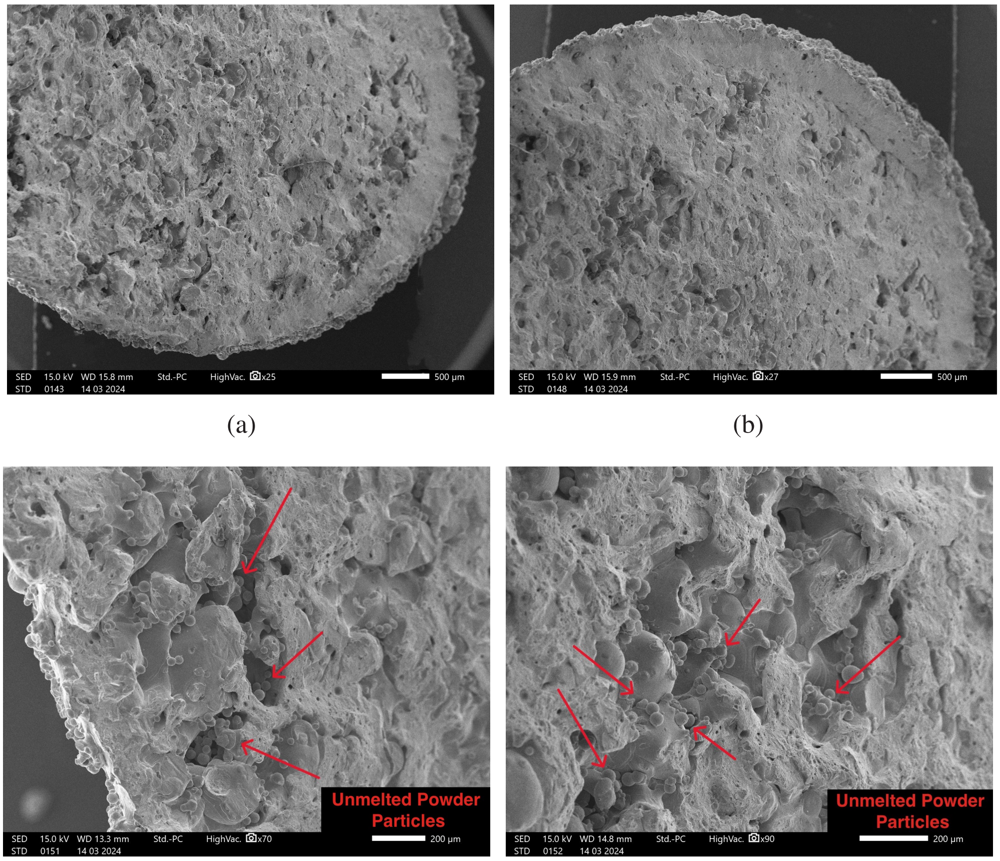

(a) (b)

(c) (d)

Figure 4.12: Fracture surface of specimen fabricated at 45°, premature failure: (a) and (b) low magnification view, (c) and (d) high magnification view, red arrows indicate unmelted powder particles

6. Fracture surface morphology

To analyze the fracture behavior of SLM-printed parts, SEM images of the fracture surface of samples fabricated at a 45° angle were obtained for two types of fracture: premature failure (Figure 4.12) and ductile fracture (Figure 4.13).

In samples with the premature failure, many areas with partially melted or unmelted powder particles were found (Figure 4.12 (c) and (d)). These powder particles are probably left between the printed layers and are caused by a lack of fusion. It has been noted in previous literature that this is one of the main causes of premature failure, causing scatter in elongation results [38, 39].

The second sample was printed in the same batch as the prematurely failed sample but showed ductile behavior. When looking at the surface morphology, it can be seen that it is significantly different from the former. It can be seen that there are almost no areas with partially melted steel powder particles. However, formation of dimples and voids (indicated by different colored arrows) can be seen throughout the surface (Figure 4.13 (b) and (c)), which are mainly verify ductile fracture of the specimen [39, 37].

Although both samples were printed under the same conditions in the same batch, there

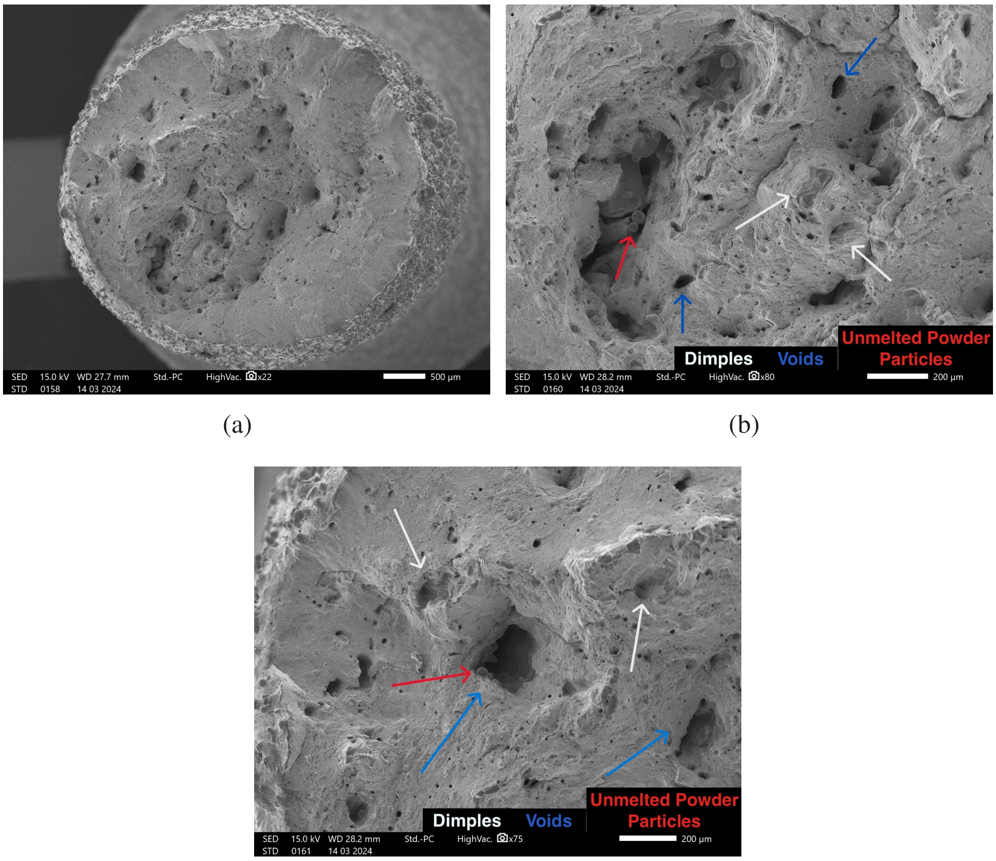

(a)

(b)

(c)

Figure 4.13: Fracture surface of specimen fabricated at 45°, ductile fracture (a) low magnification view, (b) and (c) high magnification view: red arrows indicate unmelted powder particles, blue arrows indicate voids and white arrows indicate dimples

is a difference in their fracture behavior as well as in their surface morphology. One sample exhibits a much greater lack of fusion, resulting in fracture with a low elongation, while the other has more dimples and voids, corresponding to ductile behavior. Printed samples do not give identical results as they may have defects even during printing. To reduce such results the density of the printed part should be validated in future works, also varying the printing parameters can help to control the melting so that the distribution and fusion of the powder is uniform throughout the printed layers.

4.2.2 Fatigue

1. Fatigue Behaviour in As-Built Condition

To investigate the effects of the build orientation on the fatigue performance, alternating load was applied to all the specimens, using the above-mentioned stress amplitudes (Table 3.1). Number of cycles leading to failure were recorded and plotted on an S-N curve. As per recommendations from the literature, trend lines were then created using a power formula. Number of cycles axis was then converted to a log scale, since it better displays high and low cycle fatigue together. On a regular curve, if the difference between the numbers is too big, curve would not show it properly. Low and high cycle fatigue differs in the number of cycles; low cycles present in the range from 10^0 to 10^4, while high cycle fatigue lasts for even longer, until the endurance limit is reached. As per the recommendation from the literature and the GB/T 26077-2010 standard, fatigue limit is encountered in the ranges of 10^6 to 10^7. Moreover, a study done by Wang et al showed that endurance limit for SLM printed stainless steel was encountered generally at stress levels of 0.4 and 0.6 of tensile strength, which will be our expectation [40].

HST-P50 fatigue testing machine is capable of a maximum of 20 Hz of loading frequency. During the study, this frequency was deemed too high for high stress loads, so for the stress points of over 70% of yield stress, frequency of testing was considerably lowered. The highest stress point (90%) was tested at a frequency of 1 Hz, while 80 and 70 were tested at 10 Hz. The rest were all tested at maximum possible frequency. Results of fatigue performance of as-built specimens are presented in the Figure 4.14.

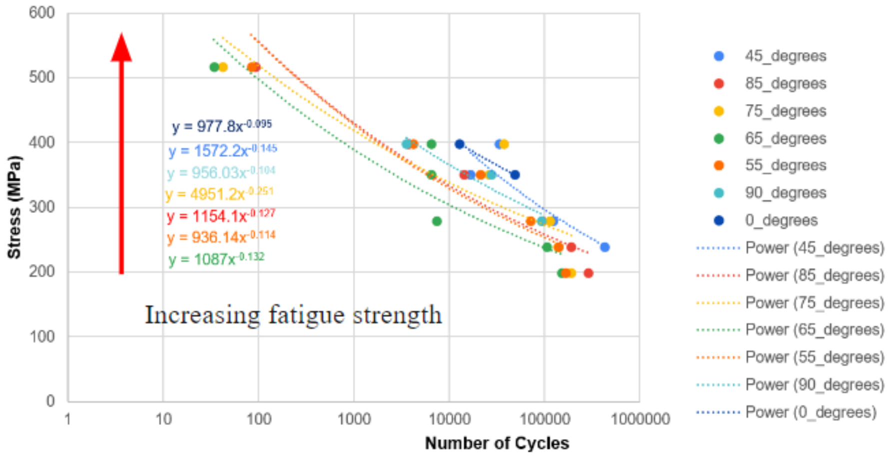

Figure 4.14: S-N curves for as-built fatigue specimens

It was found that build orientation does have an influence on fatigue performance with 45° degree specimens having highest fatigue strength and samples printed at 65° degrees being weakest. One of the anomalies encountered is that as can be seen from Table 4.5, 65° specimens in as-built condition had relatively similar number of cycles till failure for three different stress levels: 70%, 60%, and 50% of yield stress. This can be attributed to a high number of defects present that at relatively high stresses don't take long to propagate and lead to failure. From a direct comparison between the two, for a stress level of 40% of yield, 45° specimens lasted four times longer than samples printed at 65°. This leads to a conclusion that the difference between the two is too significant to not be a factor that influences fatigue performance considerably.

2. Fatigue Behaviour in the Heat Treated Condition

To characterize the influence of heat treatment on fatigue behaviour, new specimens were printed using the same conditions of as-built and exact same printing parameters.

For this study, no surface treatment was done as well, so roughness of the morphology was not monitored. Specimens printed at angles of 45° and 65° were tested to reveal the effect of heat treatment on fatigue. These angles were chosen as the strongest and weakest performing build orientations respectively. Results for all specimens is summarized in the Table 4.5.

Table 4.5: Results for fatigue test, where AB is as-built and HT is heat treated

$\sigma_{Amplitude}$ (MPa)	45°(AB)	45°(HT)	65°(AB)	65°(HT)	75°(AB)	85°(AB)
517- 90% of σ_Y	-	686	34	1143	42	92
398- 70% of σ_Y	33146	3563	6415	4030	37155	3754
350- 60% of σ_Y	16681	19495	6409	13541	25908	14310
279- 50% of σ_Y	122004	107962	7390	84982	113600	93278
239- 40% of σ_Y	421386	426685	104282	Inf life	136324	189691
199- 35% of σ_Y	-	-	150907	-	189507	286333

Throughout the tests, it can be noted that the endurance limit was only encountered once and that was achieved by testing a heat treated sample printed at a 65°. As-built samples never reached close enough to a 10^6 cycles even at stresses considered to be where a fatigue limit is expected to occur, that is, 40% of the yield. That is explained by the presence of defects, unmelted particles, and lack of fusion that will be displayed in the Section 5 later. From a direct comparison, heat treatment did not improve fatigue of 45° printed specimens, as the Table 4.5 shows, number of cycles are comparatively similar. On the other hand, 65° specimens, which performed weakest between as-built samples, improved after heat treatment tenfold and even achieved infinite life, outperforming 45° specimens. Figures 4.15 and 4.16 show the S-N curves for the comparison of as-built and heat treated samples.

Results indicate that the positive influence for the fatigue performance of 65° shows that heat treatment does affect fatigue strength. For example, at a stress level of 50% of the yield stress, heat treated specimens outperformed as-built samples over eleven times. However, an anomaly was encountered in view of the fatigue performance of 45° specimens, even after heat treatment, number of cycles till failure did not have any significant influence. This can be explained by the fact that weakest performing samples had too many defects present in their as-built condition, leading to drastically lowered number of cycles till failure. As it was noted in the previous section, samples printed at 65° had no notable increase in fatigue strength in the range of 70%, 60%, and 50% of yield, which is an anomaly in itself. The defects removed by heat treatment accelerated crack propagation to the point that no improvement could be seen even after lowering the amplitude of applied stress.

3. Goodman curve

The Goodman curve is often considered to be a better representation of fatigue strength, because it allows us to approximate the ratios of amplitude and mean stress that provide

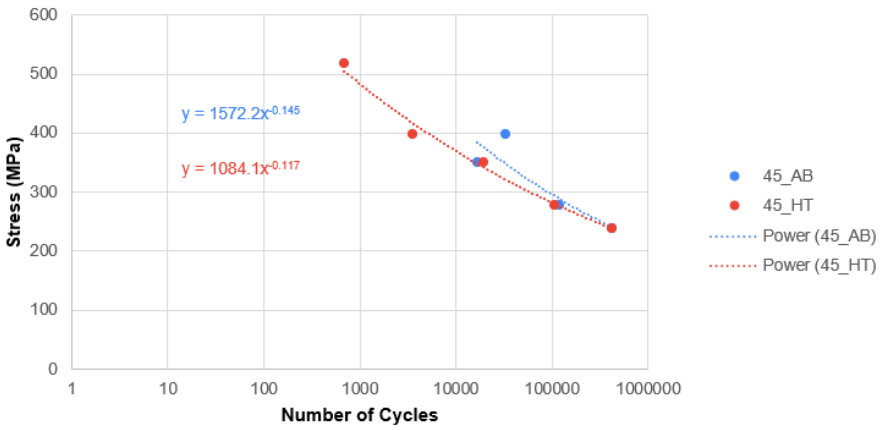

Figure 4.15: S-N curves of 45° for the comparison of as-built and heat treated specimens

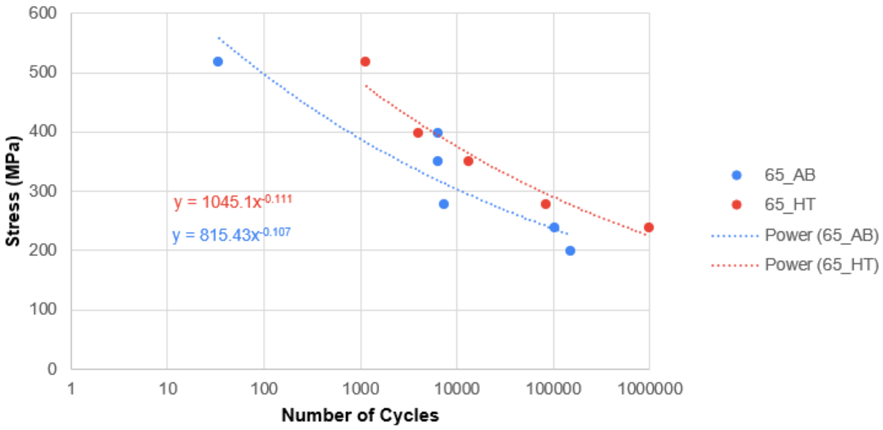

Figure 4.16: S-N curves of 65° for the comparison of as-built and heat treated specimens

finite or infinite life. This can be achieved by plotting amplitude stress on the y-axis and mean stress on the x-axis. Goodman curve is a linear curve that connects the endurance limit σ_E on the abscissa and the ultimate tensile strength σ_{UTS} of the specimen on the ordinate. From the curve on Figure 3.3, the following results were obtained: σ_{UTS}=700 MPa and σ_{Yield}=580 MPa. Taking the endurance limit of the heat treated 65° specimens, it was found to be equal to σ_E=239 MPa. Figure 4.17 displays the Goodman curve for the heat treated 65° specimens.

4. Fracture surface morphology

Surface of the fracture was analyzed using SEM imaging. Hypothesis for the anomaly of similar number of cycles to failure for three separate stress ranges was proven right, since SEM images showed an abundance in defects, like lack of fusion, unmelted powders, voids that all contribute to crack initiation sites. SEM images of specimens printed at 65° that failed after a similar number of cycles are presented in the Figure 4.18. They indicate an abundance of crack initiation sites that lead to accelerated propagation of them, resulting in faster than expected failure.

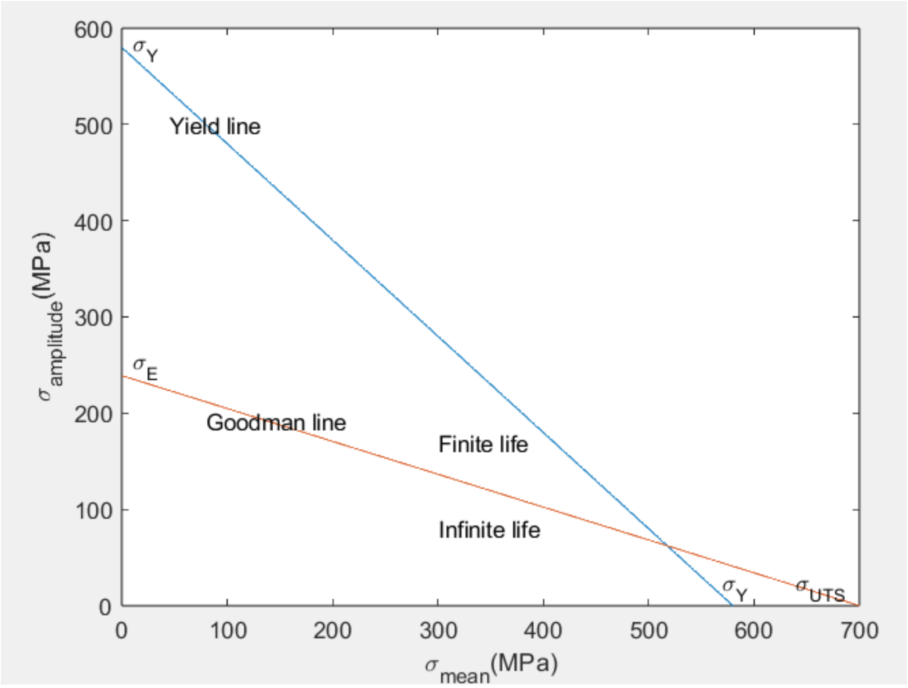

Figure 4.17: Goodman curve for a heat treated specimen printed at 65°

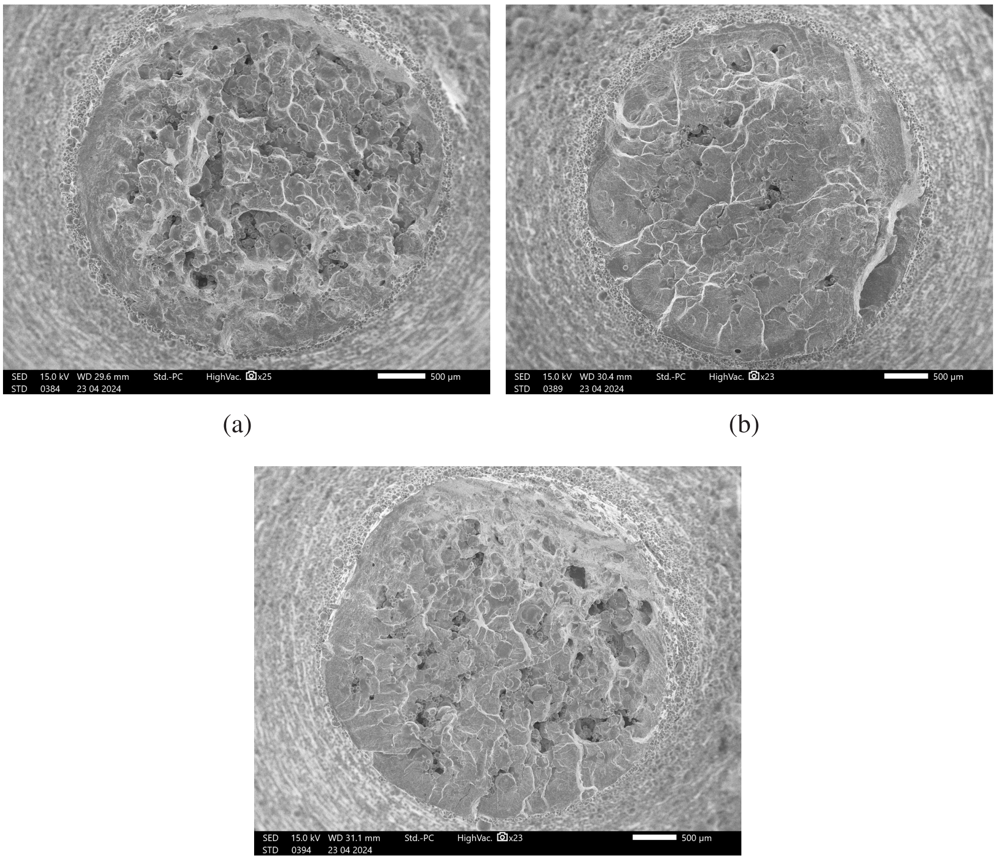

(a) (b)

(c)

Figure 4.18: Fracture surface of specimens fabricated at 65° that lasted a similar number of cycles at: (a) 70%, (b) 60%, and (c) 50% of yield.

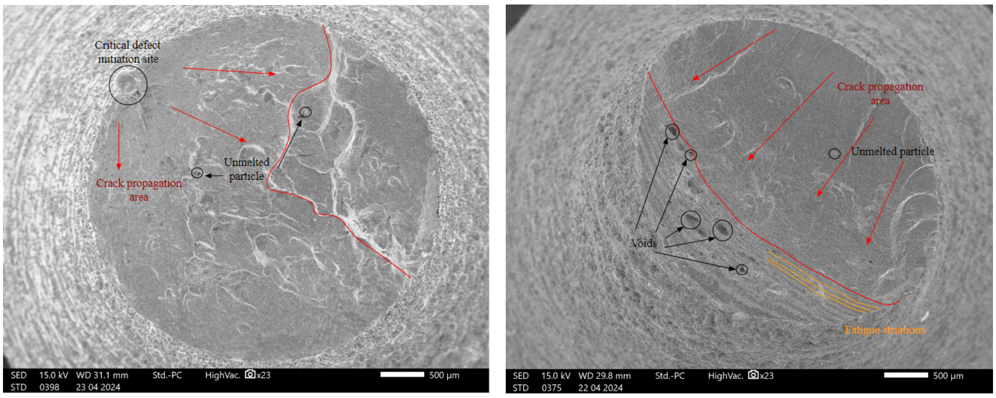

(a) (b)

Figure 4.19: Fracture surface of specimens printed at 65° in: (a) as-built and (b) heat treated conditions with highlighted defects.

Apart from that anomaly, SEM imaging revealed the effects of heat treatment in mitigating the defects. In all of the as-built specimens, number of unmelted powder particles is high, indicating that either the laser power was not high enough or laser speed was too much, so the particles were not melted properly. Heat treatment proved to reduce the number of unmelted particles, making them almost non-existent. Figure 4.19 depict this improvement that undoubtedly resulted in considerably better fatigue strength, more accurately in tenfold improvement. Figure 4.19 also highlights the crack propagation area, which is often always flat, while the failure occurs on a more uneven area. Directions of crack growth can be seen from the presence of fatigue striations. Additionally, crack growth can be traced from a crack initiation site as in Figure 4.18(a), where a critical defect can be seen in the form of an abnormally huge unmelted particle. After heat treatment, such a deformity is expected to go away, allowing for the structure to last much longer. One of the voids was investigated and a close-up look is depicted in Figure 4.20.

4.2.3 Hardness

The micro indentation test was acknowledged for its materials resistance to local plastic deformation when subjected to applied loads. This indicates that microhardness serves as a valuable measure for reconciling variations in characteristics within microstructures. The results of average microhardness values (HV) are summarized in Figure4.21. Specifically, the 90° as-built sample exhibits a gradual increase in microhardness values compared to the 0° as-printed sample. This observed pattern provides supporting evidence for the dominance of specimen softening, which is related to prolonged exposure to high temperatures [41].

SLM-printed components exhibited microhardness values ranging from 183.4 HV to 241.4 HV. The lowest microhardness, 183.4 $\pm$ 5.30 HV, was recorded for samples oriented

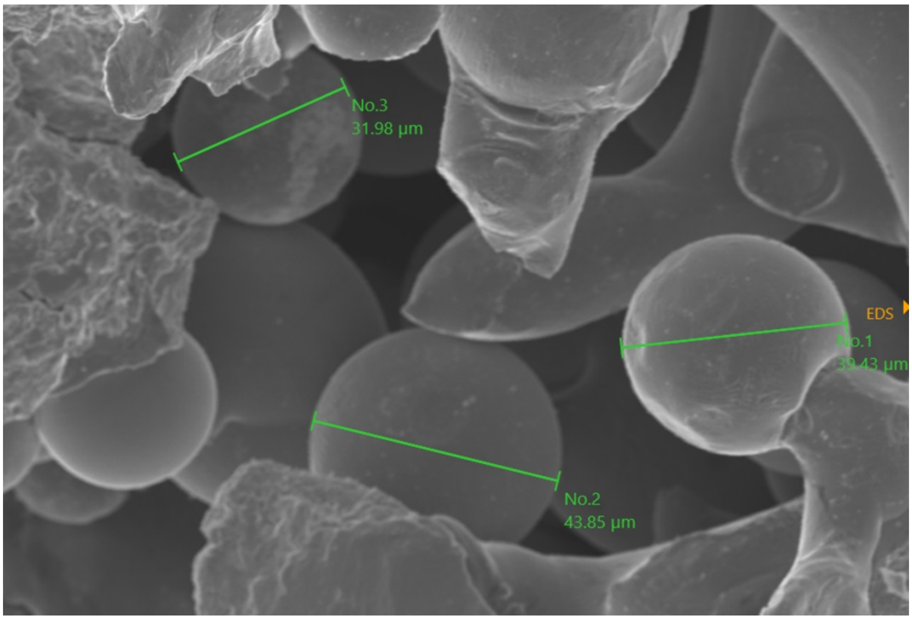

Figure 4.20: Close-up into a fracture surface of a void of an as-built specimen printed at 65° with unmelted powder particles inside

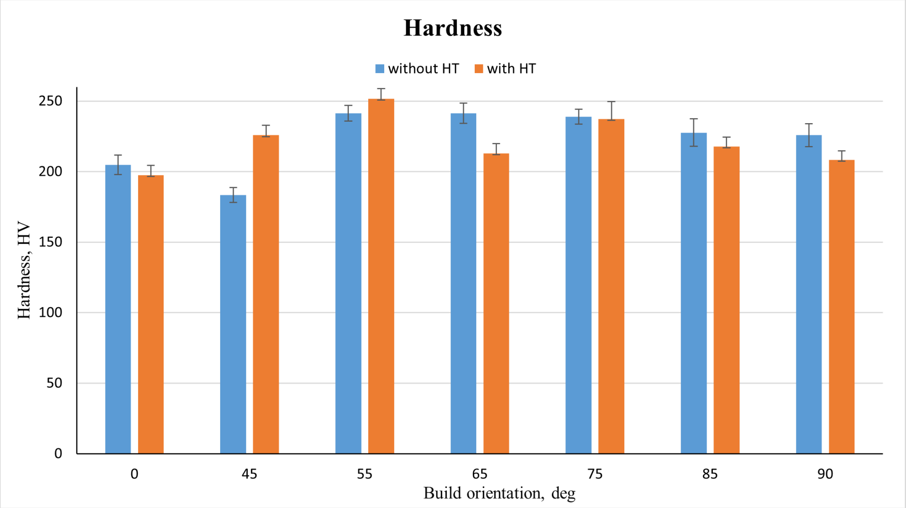

Figure 4.21: Hardness results

at 45 degrees, with minimal variations observed between specimens printed at 55 and 75 degrees. Parts printed at 85○ and 90○ displayed nearly identical hardness.

The build direction was found to have no significant impact on the microhardness of the specimens, aligning with findings from previous studies [42]. Samples printed at 0 and 45 degrees showed a slightly lower average microhardness, attributed to the coarser microstructure evident in these samples.

Additionally, the chemical composition of hardness specimens was evaluated and represented in Table 4.6. The content of all the components was found to be very identical in comparison with the powder composition, highlighting the precision and consistency of preserving chemical composition during the additive manufacturing process.

Generally, rapid heating and subsequent cooling of the workpiece during heat treatment lead to significant temperature gradients, which leads to the occurrence of residual stresses. These stresses, in turn, contribute to the deformation of the part, which ultimately negatively affects the mechanical characteristics of the additively manufactured parts [43]. According to Figure 4.21, microhardness values were determined for all specimens after heat treatment at 1000°C. The values for specimens with 0° and 90° orientation are significantly lower in comparison with as-built build orientation parts. Such difference can be attributed to coarsening of microstructure, where the sigma-ferrite phase becomes harder compared to the austenitic phase, contributing to the lowered hardness values[28].

In the case of 45° and 55° build orientation, the post-heat treatment micro-hardness results showed an increase compared to pre-treatment levels, reaching 225.8±6.93 HV and 251.6±6.52 HV, respectively. At such building orientations, the printing undergoes more pronounced layer-by-layer formation, and involves proper melting of powder and its solidification under laser energy. In comparison, the micro-hardness measurement for the specimen at a 65° orientation yielded a value of 241.4±7.18 HV, which decreased considerably to 212.9±7.25 HV after undergoing heat treatment. It is likely to be influenced by significant residual stresses primarily aligned along the building direction [44].

According to the previous studies, the cellular structure tends to disappear at heat treatment above 400, therefore there occur segregations of Mo and Cr at the cell boundaries, which is much lower compared to the as-printed condition. Such a process means that the established dislocation network gradually deteriorates after heat treatment for a set period. Thus, there is a continuous decrease in hardness values with increasing temperature of heat treatment [45].

Table 4.6: Chemical composition of printed hardness sample

Element	**Si**	**Cr**	**Mn**	**Ni**	**Mo**	**Fe**
wt%	0.85	18.56	0.63	9.74	1.71	68.51

4.2.4 Corrosion

The investigation into the effect of build orientation during SLM of the stainless steel 316L alloy included an electrochemical comparison after exposure to various sodium solutions. In Appendix C, Table C.1 and Table C.2 represent the current density, corrosion potential, and rate values of the specimens at solutions of 0.9 %wt and 3.5 %wt. The chosen concentrations reflect relevant conditions that the stainless steel might encounter in practical applications, ensuring a comprehensive assessment of its corrosion resistance under diverse environmental conditions. This investigation allows for a more nuanced understanding of the specimen's performance under different build orientations and sodium solution concentrations.

1. Open Circuit Potential

The SLM-printed working electrodes were subjected to stable polarization testing, which yielded the open circuit potential measurements (OCP). OCP is a measurement of corrosion potential that highlights the potential at which the corrosion occurs. It can also be characterized as the potential difference between the working and reference electrodes when there is no electric field applied. While OCP can not describe the kinetics of the corrosion reaction, it allows the susceptibility to corrosion to be gauged. From the literature review, it was reported that the increase in OCP values indicates the increased compactness of the passive film with time [46].

OCP results graphed as a function of time can be seen in Figure 4.22. Almost all of the as-built specimens experienced an increasing trend in the values of OCP, which indicates increased compactness of the passive film. Additionally, the higher the OCP value, the more stable the material and less prone to corrosion, meaning that it possesses a low corrosion tendency [31]. Judging from the graphs of OCP values against time, it was found that all the specimens before heat treatment experienced an increase in OCP immersed in both concentrations of salt.

At a concentration of 3.5 %wt of NaCl solution, the highest OCP values were recorded at -0.10255 V for specimens printed at 45 degrees, while the lowest value of -1.1073 V was observed for specimens printed at 55 degrees. This decrease in voltage indicated these samples underwent a decrease in the compactness of their passive film. A similar pattern can be seen for the minimum OCP reached with the 55-degree specimen in 0.9wt NaCl, which was measured at -0.24605 V.

Similar polarization measurements are carried out for both concentrations after heat treatment and results are represented in Figure 4.22. The obtained graphs display a decreased pattern, indicating a decline in compactness of passive film in 7200 seconds, and this decreased value means susceptibility of the stainless steel after heat treatment. Heat-treated specimens take less time for stabilization in comparison to as-built stainless steel, and the final potential value becomes more negative. Such decline can happen due to the porosity of the specimen, leading to the intensive chemical reaction of corrosion on the surface.

A slight difference in OCP value for different build orientations can be observed, and it ranges from -0.26 V to -0.29 V. Comparing the results of as-built specimens at 3.5 %wt NaCl concentration, highest OCP were recorded at 45-degree at -0.10255 V, while after heat treatment it was decreased to -0.29714 V. Several studies relate this phenomenon with breakdown of protective oxide on the steel surface after anodic polarization of the steel [47].

2. Potentiodynamic testing

In general, current density, $I_0(A/cm^2)$ can be defined as the rate at which the stainless-steel specimen corrodes in sodium chloride, showing a flow of electric current during

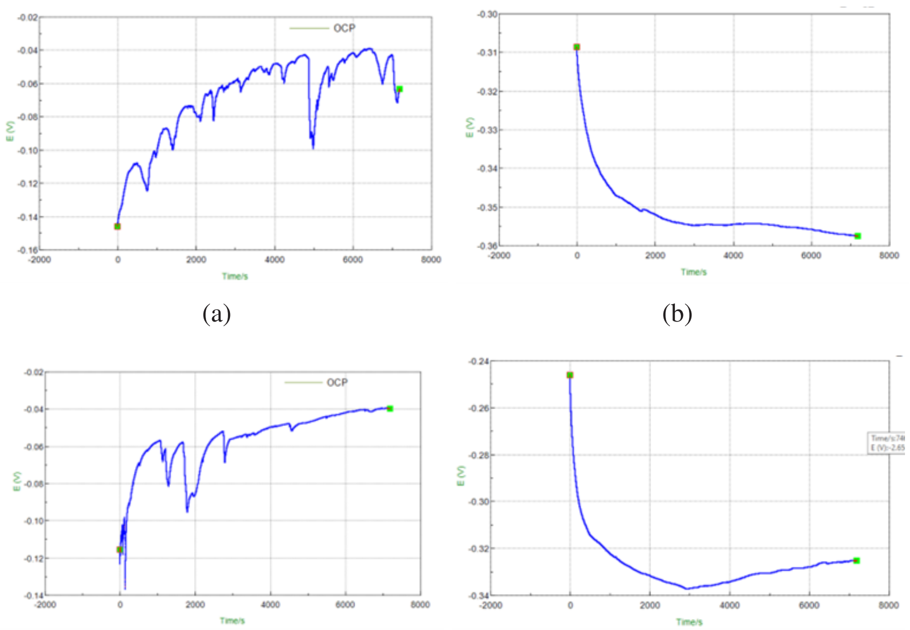

(a) (b)

(c) (d)

Figure 4.22: Open circuit potential graphs of 0-degree printed specimen (a) 0.9M before HT; (b) 0.9M after HT; (c) 3.5M before HT; (d) 3.5M after HT

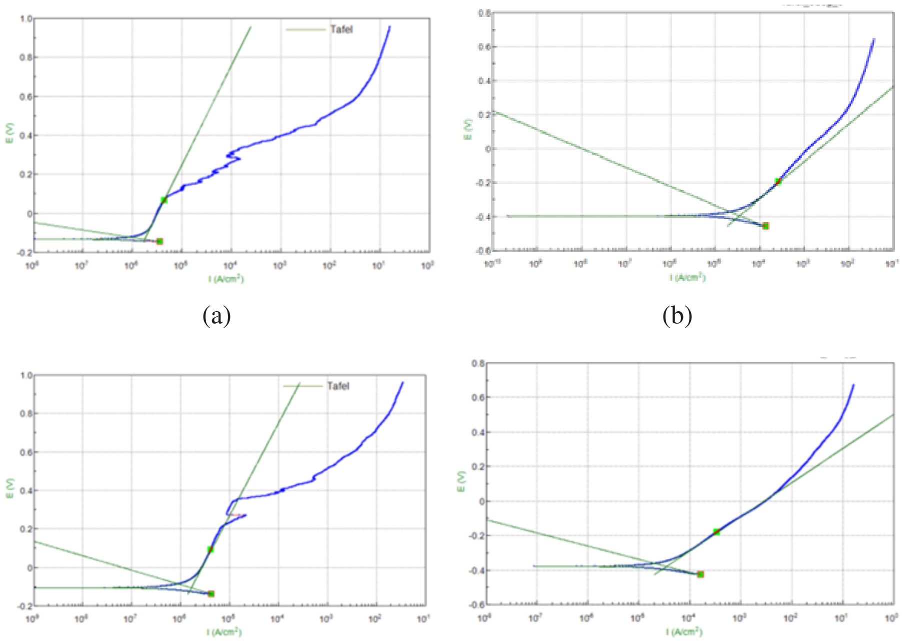

(a) (b)

(c) (d)

Figure 4.23: Open circuit potential graphs of 0-degree printed specimen (a) 0.9M before HT; (b) 0.9M after HT; (c) 3.5M before HT; (d) 3.5M after HT

the electrochemical reaction on the surface of the metal. The higher the current density, the faster the corrosion will be. By comparing the I_0 values at different sodium chloride concentrations, at higher sodium concentrations the current density becomes higher, and the corresponding corrosion rate is higher. At a 65-degree as-printed specimen, I_0 equals 7.1592E-7 and its corrosion rate is 0.0081799 mm/a at 0.9wt NaCl solution when NaCl concentration increases, the current density becomes 1.438E-5 A/cm^2 and its rate is at 0.164 mm/a.

The highest values of current density are observed in the 55-degree as-printed specimen with a 0.9M solution, yielding 1.632E-6 A/cm^2, and in the 65-degree as-built specimen with a 3.5M solution, yielding 1.438E-5 A/cm^2.

Heat treatment results displayed increased current densities, leading to higher corrosion rates. Potentiodynamic measurements at both concentrations showed that heat treatment reduces the resistance of the steel to localized corrosion pits, judging from the values of pitting current and passivation potential. The highest current density was noted for the 55-degree printed specimen at 0.000108 A/cm^2 at 3.5M solution, while the obtained results for the as-built specimen was 2.973E-6 A/cm^2. The same trend for worsening corrosion behavior after heat treatment above 1000 °C was observed in a recent study, revealing that the steel is more susceptible to localized corrosion degradation, as it reduces the steel's ability to form and maintain its passive film across a broad range of potentials in the presence of corrosive ions [30]. Notably, the corrosion potential, E(V), refers to the change of potential of the working electrode, and it leads to the formation of an oxide film on the surface of the sample. In the case of potentiodynamic testing, the potential is called cathodic polarization due to the negative potential shift. Usually, the higher value of potential can reduce the driving force of the corrosion reaction; therefore, the corrosion rate is more likely to be less. The maximum value of potential occurs at a 75-degree as-printed specimen, immersed in 0.9 %wt NaCl concentration, at -0.0318 V. It can be related to the reduction of force in the corrosion reaction, meaning that metal with high corrosion potential can lose the electrons, making it easy for stainless steel to undergo the oxidation process.

As the pitting corrosion involves the dissolution of metal, it occurs at the metal surface between the anode and cathode. The obtained results demonstrate an increase of potential with a decrease of sodium concentration at specimens printed from 55° to 90°, suggesting overall enhancement in the corrosion performance of stainless steel 316L in NaCl solution. Its value ranges from -0.099 V to -0.0625 V in a 0.9M NaCl solution and from -0.1246 V to -0.1167 V in a 3.5M NaCl solution.

Comparing these results after heat treatment, the corrosion potential has an increased result with the increasing concentration of NaCl solution, ranging from 0.9 M to 3.5 M NaCl concentration. This notable variation in corrosion potential can be attributed to the increasing presence of Cl^- ions, which in turn stimulate greater dissolution of iron. The

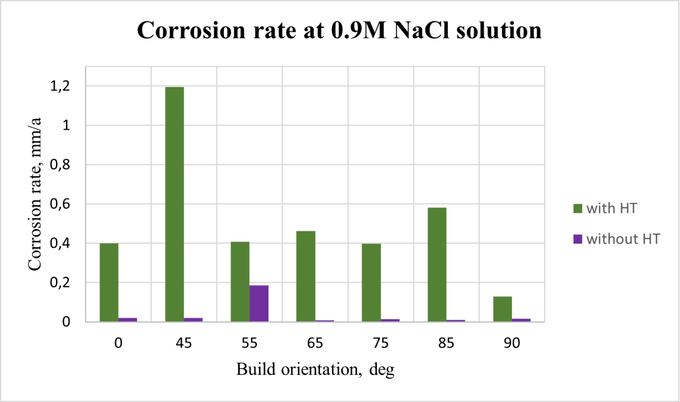

(a)

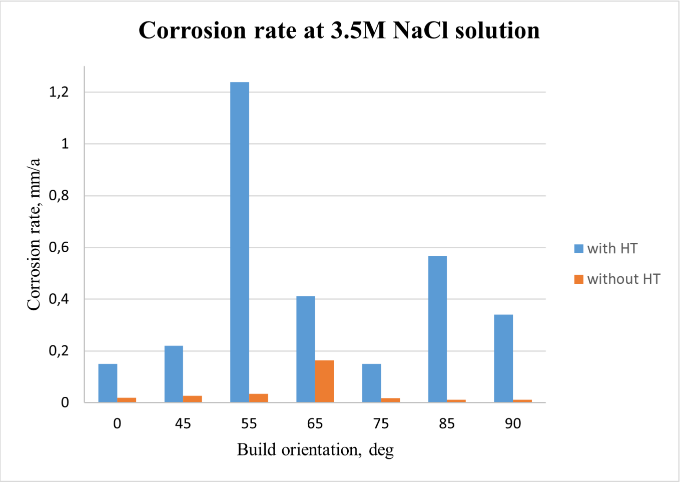

(b)

Figure 4.24: Corrosion rate changes before and after heat treatment for (a) 0.9wt% and (b) 3.5wt% NaCl solution

anodic polarization curves of the SLM-printed samples exhibit a distinct passive region [48]. Heat-treated specimens at different solutions give controversial values, and at 0.9M NaCl solution experiences an increase in corrosion potential, varying from -0.3985 V to -0.2124 V, while at higher concentrations, the voltage variation is less pronounced, typically ranging between -0.31 to -0.43 V, indicating a more stabilized corrosion potential within this concentration range. Changes in microstructure due to heat treatment can create areas susceptible to localized corrosion, which can affect the overall corrosion potential.

This observation leads to the explanation for the change in corrosion rates at different seawater environments, and Tafel curves for 0-degree printed specimens are given in Figure4.23. In investigating the corrosion behavior of stainless steel 316L, at as-built specimen of a 65-degree angle, the lowest corrosion rate, i, is measured at 0.0081 mm/a at 0.9M NaCl solution, indicating metal cation migration and the formation of a passive film. Conversely, the same working electrode demonstrates the highest corrosion rate of 0.16432 mm/a at increased concentration. It potentially can be linked to Mo-rich sub-grain boundaries acting as cathodic sites [44].

Generally comparing the results of corrosion rate at different concentrations of NaCl solution, the minimum rate of corrosion was found in the sample as-printed at 90 degrees, measured at 0.0108 mm/a at 3.5 %wt of seawater. It means that in comparison to other orientations, the layer deposition in samples printed at 90 degrees may produce the microstructure that is more corrosion-resistant. This behavior can be also explained by a higher concentration of hydroxides in the passive film, fostering more effective adsorption of Cl- ions on the passive film surface [31].

Comparing the results of heat-treated specimens in a 0.9M NaCl solution, the highest corrosion rate was observed in specimens treated at 45 degrees, while the lowest rate was found in those treated at 90 degrees. Specifically, the corrosion performance worsened after heat treatment, aligning with studies that confirm heat treatment above 1000° C leads to more grain boundaries susceptible to pitting corrosion [48].

At 3.5M NaCl solution, a 55-degree printed specimen experienced the highest corrosion rate at 1.239 mm/a, which may also be linked to the presence of a very fine austenitic structure following prolonged high-temperature thermal treatment. The specimen printed at 75 degrees, which has initially the smallest corrosion rate before heat treatment, exhibited also less prone to a level of corrosion pitting. This result is confirmed with microstructural changes that the annihilation of cellular structures does not compromise the protective oxide film.

3. Surface Morphology

Figure 4.25 depicts the corrosion characteristics of the stainless steel 316L alloy fabricated through SLM before heat treatment under various conditions. It can be noticed that the specimen displayed more prominent pitting corrosion at a concentration of 3.5%wt. It can be related to surface defects as a contributing factor to increased susceptibility for corrosion in stainless steel. This is attributed to the promotion of electrolyte stagnation in pitting areas, which is believed to influence the occurrence of localized corrosion. These localized pitting are evident in the corroded surfaces of the specimens, mostly occurring around the porosity and breaking out the passive film.

The morphology of SLM-printed samples at 0.9%wt and 3.5%wt NaCl solution is displayed and there are large severe corrosion pits at higher concentration of NaCl. These severe corrosion areas are likely to appear at the grain boundaries [49]. The anions, Cl^{-}, are being acted aggressively in the base media and in this case the localized attack of the passive layer can be seen in various depths. The SLM-printed specimen at 90 degree at a concentration of 3.5%wt NaCl is subjected to the formation of holes on the surface of metal, while the same degree samples at 0.9%wt are less keen on deposit of cavities, leading to the microstructural heterogeneities.

Surface morphology after heat treatment can be seen in same Figure 4.25. The same trend remained where on the surface of the specimen there are more corrosion pits at higher concentration of NaCl. Comparing the SEM images of 55-degree printed parts,

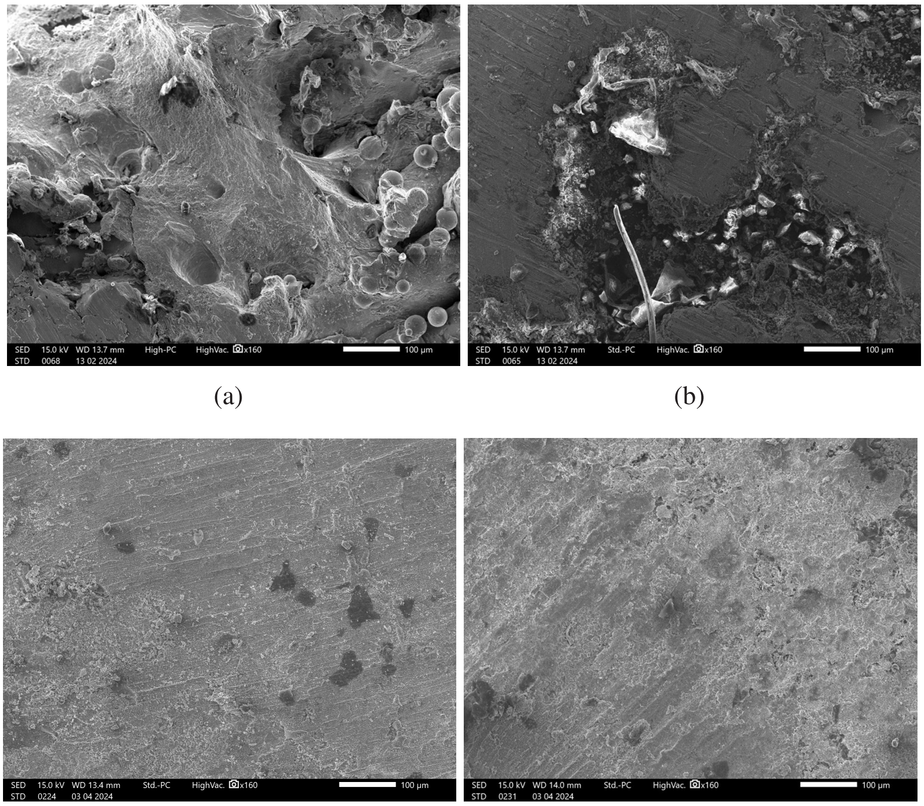

(a) (b)

(c) (d)

Figure 4.25: Post-corrosion morphology 55 degree printed stainless steel 316 (a) 0.9M NaCl solution without HT; (b) 3.5M NaCl solution without HT; (c)0.9M NaCl solution with HT; (d) 3.5M NaCl solution with HT;

the formation of holes on the surface of metal is obviously displayed at 3.5%wt NaCl solution, while the same degree samples at 0.9%wt NaCl solution are less keen on deposit of cavities. This claim is also supported by corrosion rate, which was 0.407 mm/a and 1.239 mm/a, respectively.

Chapter 5: Conclusion and future work

The first part of the capstone project has investigated the rheological properties of stainless-steel powder from two different suppliers and the mechanical performances of SLM printed parts. Through a comprehensive analysis of rheological and mechamical properties, the following conclusions were made:

- Both powders indicated excellent flowability, deeming them ideal for SLM printing. However, atomized powder provided by supplier 1 (S1) performed better in almost every test. SEM analysis indicated that S1 powder has more spherical and homogeneous particles, that is, particle sizes are close to one another.PSD analysis reported a smaller span for S1 powder, which means efficient particle packing and powder homogeneity. According to the angle of internal friction S1 powder requires less energy for it to become aerated, which indicates that it is less cohesive and thus better able to flow.According to the flowability indicators discussed within this capstone report, both powders displayed an exceptional level of flowability, with some of the tests reporting similar results as in bulk density and Hausner ratio.

- Tensile testing results showed that build orientation relative to the printing platform does not have a significant effect on UTS of SLM fabricated 316L stainless steel parts. However, inclusion of heat treatment significantly increased the UTS of samples built horizontally (parallel to the loading direction). In general, the samples became more ductile after heat treatment. Analysis of the fracture surface of the as build and heat-treated samples showed that after heat treatment there are significantly fewer pores and unmelted powder particles on the fracture surface, which enhanced the elongation and toughness of samples. Analysis of the fracture surface morphology of samples from the same batch but with different fracture types showed that inconsistencies can occur even in the printing process. A significant lack of fusion was observed, leading to premature failure of parts.

- Fatigue tests revealed that build orientation has a significant effect with 45° specimens outperforming the rest in as-built condition. An anomaly was encountered in view of fatigue not improving after reducing the applied stress, attributed to the overwhelming effect of defects. Heat treatment improved fatigue strength for 65° specimens tenfold, while did not have a significant effect on 45° samples. Despite such conflicting results, structure improved a lot due to the reduction of the number of defects in the form of unmelted particles, voids, and lack of fusion.

- From the hardness test results, it was reported that the lowest microhardness values were found for 45° as-printed specimens, whereas samples printed at 55 and 65 degrees relative to the printing platform performed the best. After heat treatment, the specimen at 0° showed decreased hardness properties, and thermal treatment gives no significant impact on the microhardness of the specimen.

- Regarding the corrosion behavior of SLMed specimens, the corrosion potential gradually decreases, while the corrosion current density gradually increases with an elevated concentration of NaCl in the solution. It reveals that the corrosion process accelerates with a higher concentration of NaCl. Heat treating at 1000°C resulted in minor pits with shallow depths, and subsequent thermal treatment significantly altered the microstructure of SLM 316L stainless steel. In a 3.5M NaCl solution, the specimen printed at 55° experienced the highest corrosion rate possibly due to the fine austenitic structure resulting from prolonged high-temperature treatment. Interestingly, the specimen printed at 75°, initially showing the lowest corrosion rate before heat treatment, also displayed less susceptibility to corrosion pitting.

Investigation of the mechanical performances showed that mechanical properties of the SLM fabricated parts are affected by the residual stresses left from support structures and high-temperature gradient due to high cooling rate. Those heat treatment process enhances overall mechanical performance. On another side, the properties of the material before heat treatment should be studied deeper, since during the printing process there may be different defects, such as lack of fusion, voids, and cavities. To mitigate these issues, in future works measuring the density of parts to get information on internal defects should be considered.

Bibliography

[1] P. Qiao and M. Yang, "Fatigue life prediction of pultruded e-glass/polyurethane composites," *Journal of Composite Materials*, 2006.

[2] K. Kakaei, M. D. Esrafili, and A. Ehsani, *Graphene and Anticorrosive Properties*. Interface Science and Technology, 2019.

[3] H. Rainer, "Viewpoint: Metallurgical aspects of powder bed metal additive manufacturing.," *Materials of Science*, 2016.

[4] H. Panchal, D. Bhaliya, and M. Pate, "Powder manufacturing techniques: A review," *International Journal of Research and Review*, 2023.

[5] A. Baskoro, S. Supriadi, and D. Dharmanto, "Review on plasma atomizer technology for metal powder," *MATEC Web of Conferences*, 2019.

[6] J. Wu, M. Xia, J. Wang, B. Zhao, and C. Ge, "Effect of electrode induction melting gas atomization on powder quality: Satellite formation mechanism and pressure," *Materials*, 2023.

[7] Y. Cui, Y. Zhao, H. Numata, H. Bian, K. Wako, K. Yamanaka, K. Aoyagi, C. Zhang, and A. Chiba, "Effects of plasma rotating electrode process parameters on the particle size distribution and microstructure of ti-6al-4 v alloy powder," *Powder Technology*, 2020.

[8] J. Weaver, J. Whiting, V. Tondare, C. Beauchamp, M. Peltz, J. Tarr, T. Phan, and A. Donmez, "The effects of particle size distribution on the rheological properties of the powder and the mechanical properties of additively manufactured 17-4 ph stainless steel," *Additive Manufacturing*, 2021.

[9] Y. Zhao, Y. Cui, Y. Hasebe, H. Bian, K. Yamanaka, K. Aoyagi, T. Hagisawa, and A. Chiba, "Controlling factors determining flowability of powders for additive manufacturing: A combined experimental and simulation study," *Powder Technology*, vol. 393, pp. 482–493, 2021.

[10] M.Z.Gao, B.Ludwig, and P. Todd, “Impact of atomization gas on characteristics of austenitic stainless steel powder feedstocks for additive manufacturing,” *Powder Technology*, 2020.

[11] N. Yan, T. Junjie, B. Yang, Q. Lei, Y. Shu, and L. Yunping, “Comparison in characteristic and atomization behavior of metallic powders produced by plasma rotating electrode process,” *Advanced Powder Technology*, 2020.

[12] I. E. Anderson, E. M. White, and R. Dehoff, “Feedstock powder processing research needs for additive manufacturing development,” *Current Opinion in Solid State and Materials Science*, vol. 22, pp. 8–15, 2018.

[13] L. Bochuan, W. Ricky, T. Christopher, A. Ian, and H. Richard, “Investigaztion the effect of particle size distribution on processing parameters optimization in selective laser melting process,” *2011 International Solid Freeform Fabrication Symposium*, 2011.

[14] K. Muhammad Ali, A. Muhammad Zubair, K. Mushtaq, I. J. Syed Husain, and R. Badar, “An experimental investigation on accuracy of Hausner Ratio and Carr Index of powders in additive manufacturing processes,” *Metal Powder Report*, vol. 76, 2021.

[15] K. Parnian, S. B. Umberto, A. D. Dupuy, M. Kaka, and J. M. Schoenung, “A statistical analysis of powder flowability in metal additive manufacturing,” *Advanced Engineering Materials*, 2020.

[16] E. Abdullah and D. Geldart, “The use of bulk density measurements as flowability indicators,” *Powder Technology*, vol. 102, pp. 151–165, 1999.

[17] A. Stavrou, C. Hare, and A. Hassanpour, “Investigation of powder flowability at low stresses: Influence of particle size and size distribution.,” *Powder Technology*, vol. 364, 2020.

[18] M. A. Spurek, H. Lukas, W. Christian, A. B. Spierings, J. H. Schleifenbaum, and K. Wegener, “Influence of the particle size distribution of monomodal 316L powder units flowability and processability in powder bed fusion.,” *Progress in Additive Manufacturing.*, 2020.

[19] R. P. Zou and A. B. Yu, “Evaluation of the packing characteristics of mono-sized non-spherical particles.,” *Powder Technology*, 1996.

[20] M. Güden, H. Yavasand, A. A. Tanrıkulu, A. Tasdemirci, B. Akın, S. Enser, A. K. Burcu, and A. Hamat, “Orientation dependent tensile properties of a selective-laser-melt 316L stainless steel,” *Materials Science and Engineering A*, 2021.

[21] K. T. Kim, “Mechanical performance of additively manufactured austenitic 316L stainless steel,” *Nuclear Engineering and Technology*, 2022.

[22] A. Deev, P. Kuznetcov, and S. Petrov, “Anisotropy of mechanical properties and its correlation with the structure of the stainless steel 316L produced by the slm method,” *Physics Procedia*, 2016.

[23] P. Wood, T. Libura, Z. L.Kowalewski, G. Williams, and A. Serjouei, “Influences of horizontal and vertical build orientations and post-fabrication processes on the fatigue behavior of stainless steel 316l produced by selective laser melting,” *Materials*, 2019.

[24] A. Avanzini, “Fatigue behavior of additively manufactured stainless steel 316l,” *Materials*, 2023.

[25] B. Blinn, M. Klein, C. Gläßner, M. Smaga, J. C. Aurich, and T. Beck, “An investigation of the microstructure and fatigue behavior of additively manufactured aisi 316l stainless steel with regard to the influence of heat treatment,” *Materials*, 2018.

[26] T. B. Primus, Z. Pitrmuc, Šimota Jan, and P. Zeman, “Laser polishing of additively manufactured 316L stainless steel with different construction angles,” *Materials and Design*, vol. 198, 2021.

[27] C. Nan, M. Guoqiang, Z. Wanquan, G. Andrew, S. Zhijian, W. Guilin, and H. Xiaoxu, “Enhancement of an additive-manufactured austenitic stainless steel by post-manufacture heat-treatment,” *Materials Science and Engineering*, 2019.

[28] K. Nurul, W. Harun, K. N. Zalikha, A. Faiz, I. Muhammad, and S. Safian, “Effect of heat treatment on mechanical properties and microstructure of selective laser melting 316L stainless stee,” *IOP Conference Series: Materials Science and Engineering*, 2017.

[29] G. Sander, X. G. A.P. Babu, D. Jiang, and N. Birbilis, “On the effect of build orientation and residual stress on the corrosion of 316L stainless steel prepared by selective laser melting,” *Corrosion Science*, 2021.

[30] J. Trelewicz, G. Halada, and O. Donaldson, “Microstructure and corrosion resistance of laser additively manufactured 316L stainless steel,” *JOM*, vol. 68, 2016.

[31] N. Jingjing, W. Liang, J. Ying, L. Qian, and L. Hongjie, “Corrosion mechanism of additively manufactured 316L stainless steel in 3.5 wt.

[32] E. Salah, M. Brikaa, C. Letenneura, D. Alex, and B. Vladimir, “Influence of particle morphology and size distribution on the powder flowability and laser powder bed fusion manufacturability of ti-6al-4v alloy,” *Additive Manufacturing*, 2020.

[33] J. Zegzulka, D. Gelnar, L. Jezerska, A. Ramirez-Gomez, J. Necasa, and J. Rozbroj, “Internal friction angle of metal powders,” *Metals*, 2018.

[34] T. Kurzynowski, K. Gruber, W. Stopyra, B. Kuźnicka, and E. Chlebus, “Correlation between process parameters, microstructure and properties of 316L stainless steel processed by selective laser melting,” *Materials Science and Engineering A*, 2018.

[35] M. Kumaran, V. Senthilkumar, T. Sathies, and C. J. Panicker, “Effect of heat treatment on stainless steel 316L alloy sandwich structure fabricated using directed energy deposition and powder bed fusion,” *Materials Letters*, 2022.

[36] L. M. Sistiaga, S. Nardone, C. Hautfenne, and J. V. Humbeeck, “Effect of heat treatment of 316L stainless steel produced by selective laser melting (SLM),” 2016.

[37] W. S. Shin, B. Son, W. Song, H. Sohn, H. Jang, Y. J. Kim, and C. Park, “Heat treatment effect on the microstructure, mechanical properties, and wear behaviors of stainless steel 316L prepared via selective laser melting,” *Materials Science and Engineering A*, 2021.

[38] R. Casati, J. Lemke, and M. Vedani, “Microstructure and fracture behavior of 316L austenitic stainless steel produced by selective laser melting,” *Journal of Materials Science and Technology*, 2016.

[39] H. Rafi, N. Karthik, H. Gong, T. L. Starr, and B. E. Stucker, “Microstructures and mechanical properties of Ti6Al4V parts fabricated by selective laser melting and electron beam melting,” *Journal of Materials Engineering and Performance*, 2013.

[40] Z. Wang, S. Yang, Y. Huang, C. Fan, Z. Peng, and Z. Gao, “Microstructure and fatigue damage of 316l stainless steel manufactured by selective laser melting (slm),” *Materials*, 2021.

[41] X. Zongyu, D. Yu, O. Xiaoqin, N. Song, and S. Min, “The effect of building direction on microstructure and microhardness during selective laser melting of ti6al4v titanium alloy,” *Materials Engineering and Performance*, 2020.

[42] I. Tolosa, F. Garciandía, F. Zubiri, F. Zapirain, and A. Esnaola, “Study of mechanical properties of AISI 316 stainless steel processed by “selective laser melting”, following different manufacturing strategies,” *International Journal of Advanced Manufacturing Technology*, 2010.

[43] A. Yadollahi, N. Shamsaei, S.M.Thompson, and M.D.Seel, “Effects of process time interval and heat treatment on the mechanical and microstructural properties of direct laser deposited 316L stainless steel,” *Materials Science and Engineering*, 2015.

[44] M. Cheng, D. Zhiwei, Z. Cui, D. Chaofang, D. Kong, Liu, Tingting, C. Shougang, and W. Xin, "The effect of sub-grain structure on intergranular corrosion of 316L stainless steel fabricated via selective laser melting," *Materials Letters*, 2019.

[45] M. Julia, K. Christian, O. Aleksei, Y. Yitong, M. Kamal, U. Elena, F. Sebastian, W. Sabine, and M. Vesselin, "On the heat treatment of selective-laser-melted 316L," *Journal of Materials Engineering and Performance*, 2022.

[46] W. Liang, L. Yong, L. Qian, and Cheng, "Effect of roughness on general corrosion and pitting of (FeCoCrNi)0.89(WC)0.11 high-entropy alloy composite in 3.5 wt.

[47] Loto and Roland, "Corrosion resistance study of 439L ferritic stainless steel subjected to high temperature variation," *Cogent Engineering*, 2021.

[48] B. Javier, G. R. Sonia, R. Marcelo, B. Torres, and R. Joaquin, "Effects of the heat treatment on the microstructure and corrosion behavior of 316L stainless steel manufactured by laser powder bed fusion," *Corrosion Science*, 2022.

[49] K. Gyeongbin, K. Wooseok, K. Kyungjung, and L. Tae-Kyu, "The corrosion of stainless steel made by additive manufacturing: A review," *Metals*, 2021.

Appendices

Appendix A: Shear Cell testing results

Supplier	Run	Cohesion, kPa	UYS, kPa	MPS, kPa	FF	AIF, °	BD, g/ml
S1	1	0.11	0.28	11.07	39.22	15.98	3.71
S1	2	0.21	0.55	11.59	20.99	16.74	4.91
S1	3	0.10	0.28	11.12	40.14	16.62	5.00
S2	1	0.24	0.71	11.87	16.71	22.66	4.60
S2	2	0.17	0.52	11.92	23.12	23.41	4.57
S2	3	0.12	0.37	12.02	32.85	22.84	3.43

Table A.1: FT4 Rheometer Shear Cell test results for two suppliers' powders

UYS- Unconfined Yield Strength; MPS- Major Principal Stress; FF- Flow Function Coefficient; AIF- Angle of Internal Friction; BD- Bulk Density;

Ratio	Flowability
<2	Very cohesive
2-4	Cohesive
4-10	Easy-flowing
>10	Free-flowing

Table A.2: Characterization of powder flowability according to the flow function coefficient

* Flow function is the ratio of the major principal stress to the unconfined yield strength.

Appendix B: Hardness and tensile testing results

B.1 Stress-strain curve

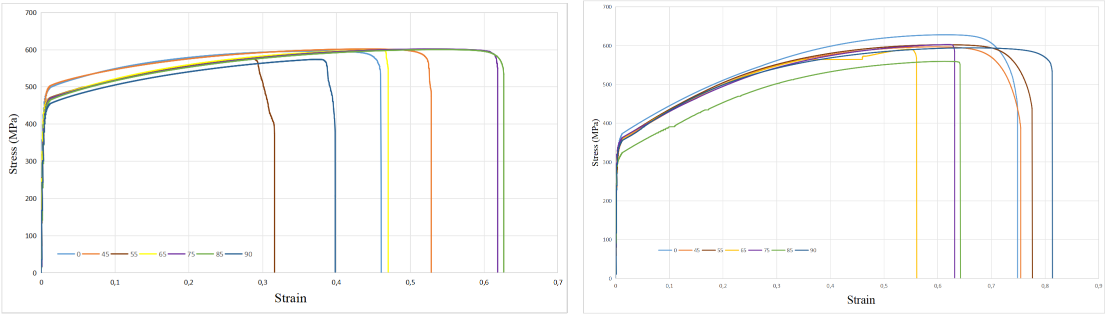

(a) (b)

Figure B.1: Stress-strain curves for all build orientations a) as build b) with heat treatment

B.2 Hardness results

Table B.1: Hardness results before HT

Angle of orientation	Hardness (HV)
0	204.8 ± 6.79
45	183.4 ± 5.30
55	241.4 ± 5.51
65	241.4 ± 7.18
75	239.0 ± 5.25
85	227.6 ± 9.71
90	225.8 ± 8.10

Table B.2: Hardness results after HT

Angle of orientation	Hardness (HV)
0	197.5 ± 7.06
45	225.8 ± 6.93
55	251.6 ± 6.52
65	212.8 ± 7.25
75	237.3 ± 12.3
85	217.9 ± 6.85
90	208.4 ± 6.29

Appendix C: Corrosion test results

C.1 Tafel curve

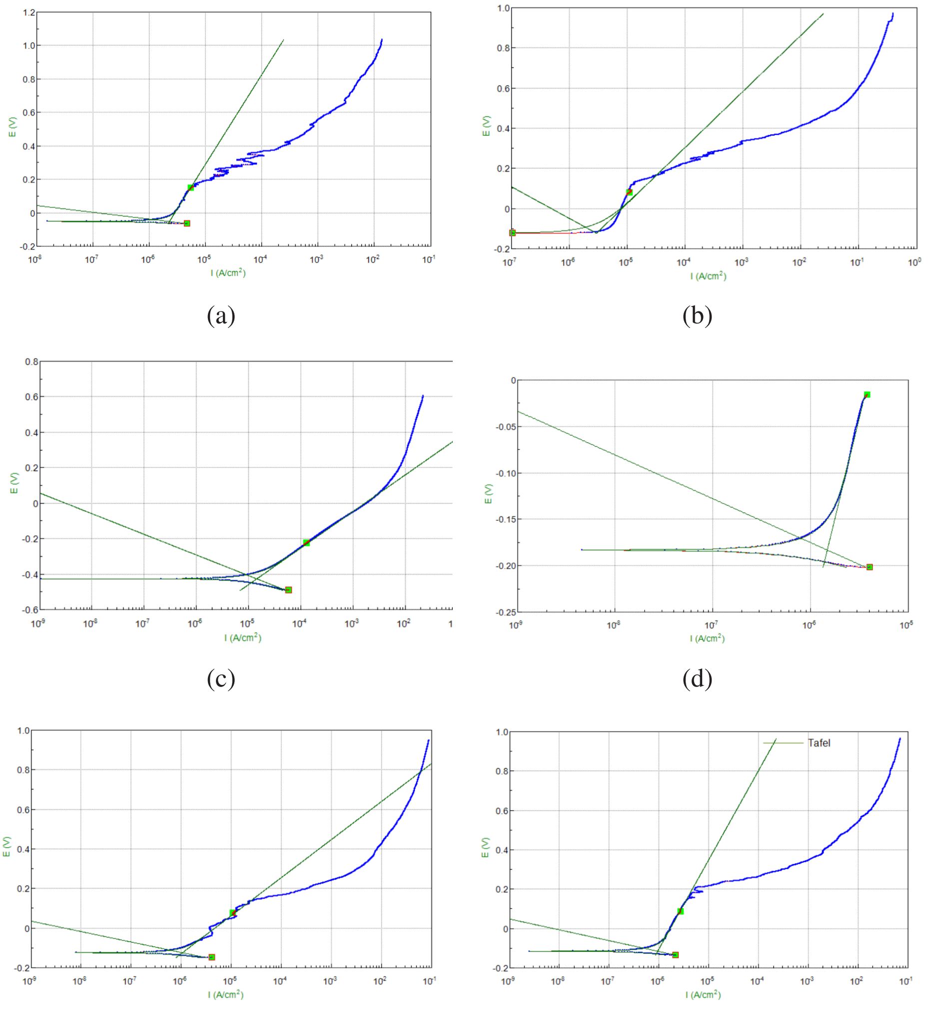

(a) (b)

(c) (d)

(e) (f)

Figure C.1: Tafel plots of SLM-printed parts for 3.5M NaCl solution before heat treatment; a) 45°, b) 55°, c) 65°, d) 75°, e) 85°, f) 90°

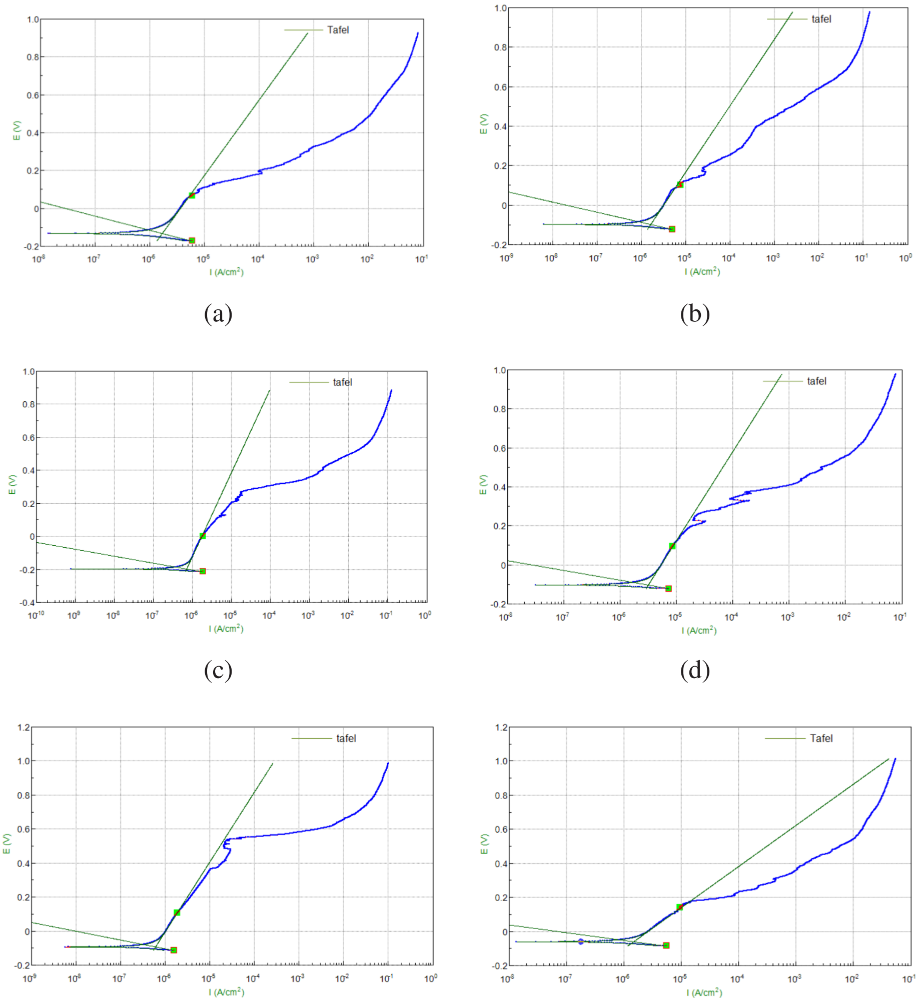

(a)

(b)

(c)

(d)

(e)

(f)

Figure C.2: Tafel plots of SLM-printed parts for 0.9M NaCl solution before heat treatment; a) 45°, b) 55°, c) 65°, d) 75°, e) 85°, f) 90°

C.2 Open circuit potential

Build orientation	Solution concentration	Current density, $I, A/cm^2$,	Corrosion potential, E_0, V	Corrosion rate, $i, mm/a$
0°	0.9M	1.74E-6	-0.134	0.0199
0°	3.5M	1.66E-6	-0.107	0.0189
45°	0.9M	1.69E-6	-0.134	0.0194
45°	3.5M	2.30E-6	-0.054	0.0262
55°	0.9M	1.63E-6	-0.099	0.1864
55°	3.5M	2.97E-6	-0.124	0.0339
65°	0.9M	7.16E-7	-0.200	0.0081
65°	3.5M	1.43E-5	-0.428	0.1643
75°	0.9M	1.19E-6	-0.032	0.0136
75°	3.5M	1.48E-6	-0.184	0.0170
85°	0.9M	9.06E-6	-0.050	0.0103
85°	3.5M	1.06E-6	-0.126	0.0121
90°	0.9M	1.48E-6	-0.063	0.0170
90°	3.5M	9.45E-7	-0.116	0.0108

Table C.1: Results of potentiodynamic testing under 0.9M and 3.5M solution before heat treatment

Build orientation	Solution concentration	Current density, $I, A/cm^2$,	Corrosion potential, E_0, V	Corrosion rate, $i, mm/a$
0°	0.9M	3.50E-5	-0.398	0.399
0°	3.5M	1.31E-5	-0.307	0.149
45°	0.9M	1.05E-4	-0.419	1.196
45°	3.5M	1.92E-5	-0.375	0.219
55°	0.9M	3.57E-5	-0.409	0.407
55°	3.5M	1.08E-4	-0.416	1.239
65°	0.9M	4.04E-5	-0.454	0.462
65°	3.5M	3.61E-5	-0.438	0.412
75°	0.9M	3.47E-5	-0.390	0.397
75°	3.5M	1.31E-5	-0.308	0.149
85°	0.9M	5.08E-5	-0.389	0.581
85°	3.5M	4.97E-5	-0.420	0.567
90°	0.9M	1.13E-5	-0.212	0.129
90°	3.5M	2.98E-5	-0.311	0.340

Table C.2: Results of potentiodynamic testing under 0.9M and 3.5M solution after heat treatment

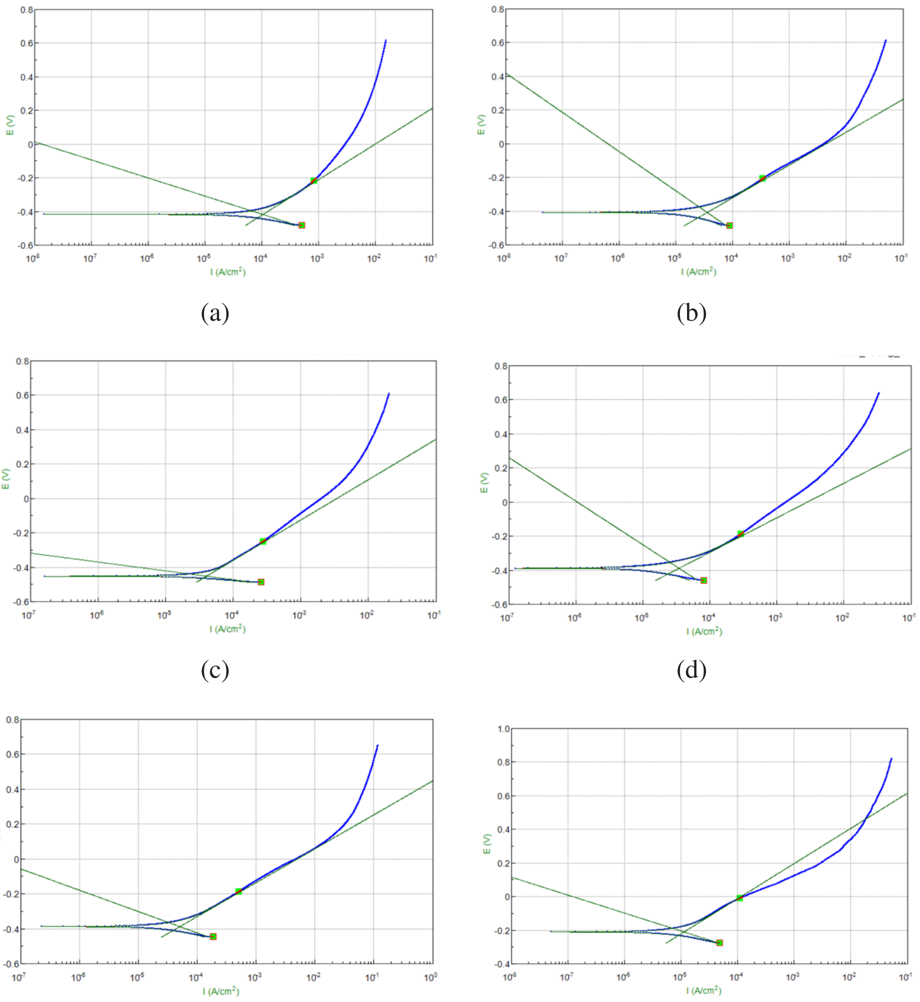

(a) (b) (c) (d) (e) (f)

Figure C.3: Tafel plots of SLM-printed parts for 0.9M NaCl solution after heat treatment; a) 45°, b) 55°, c) 65°, d) 75°, e) 85°, f) 90°

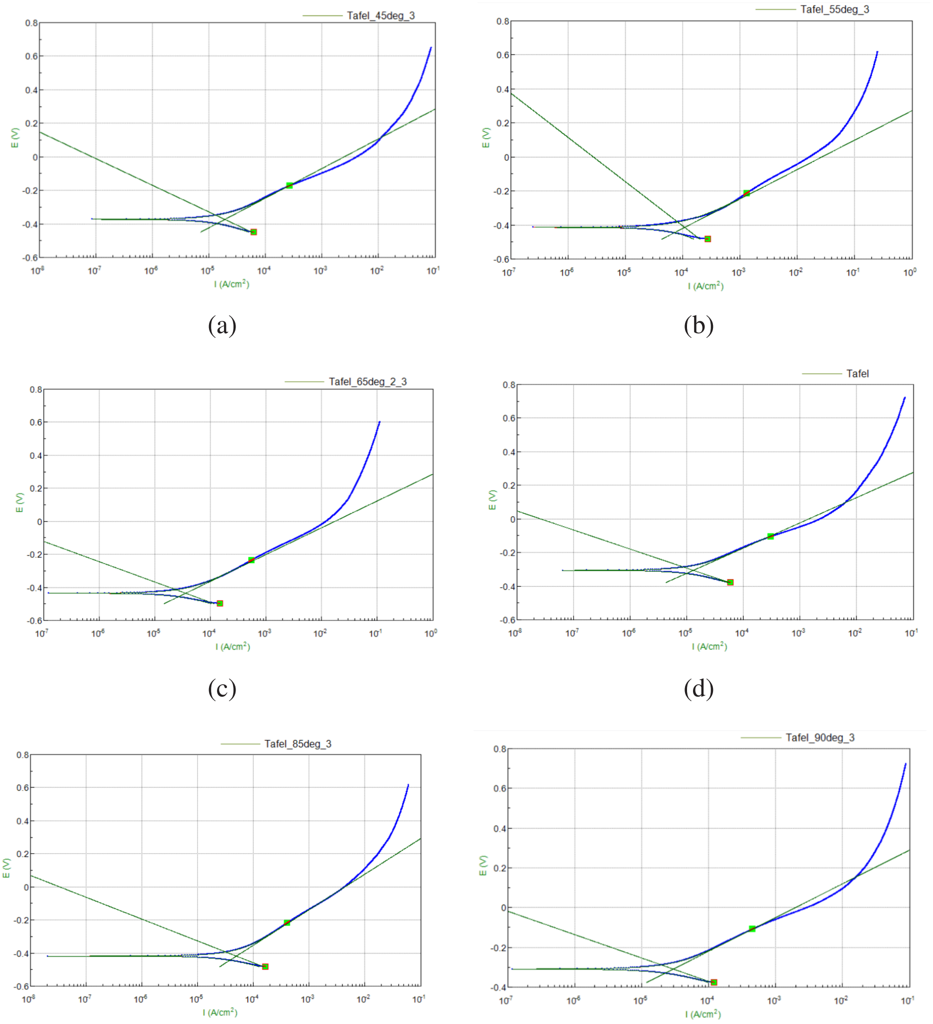

(a) (b)

(c) (d)

(e) (f)

Figure C.4: Tafel plots of SLM-printed parts for 3.5M NaCl solution after heat treatment; a) 45°, b) 55°, c) 65°, d) 75°, e) 85°, f) 85°

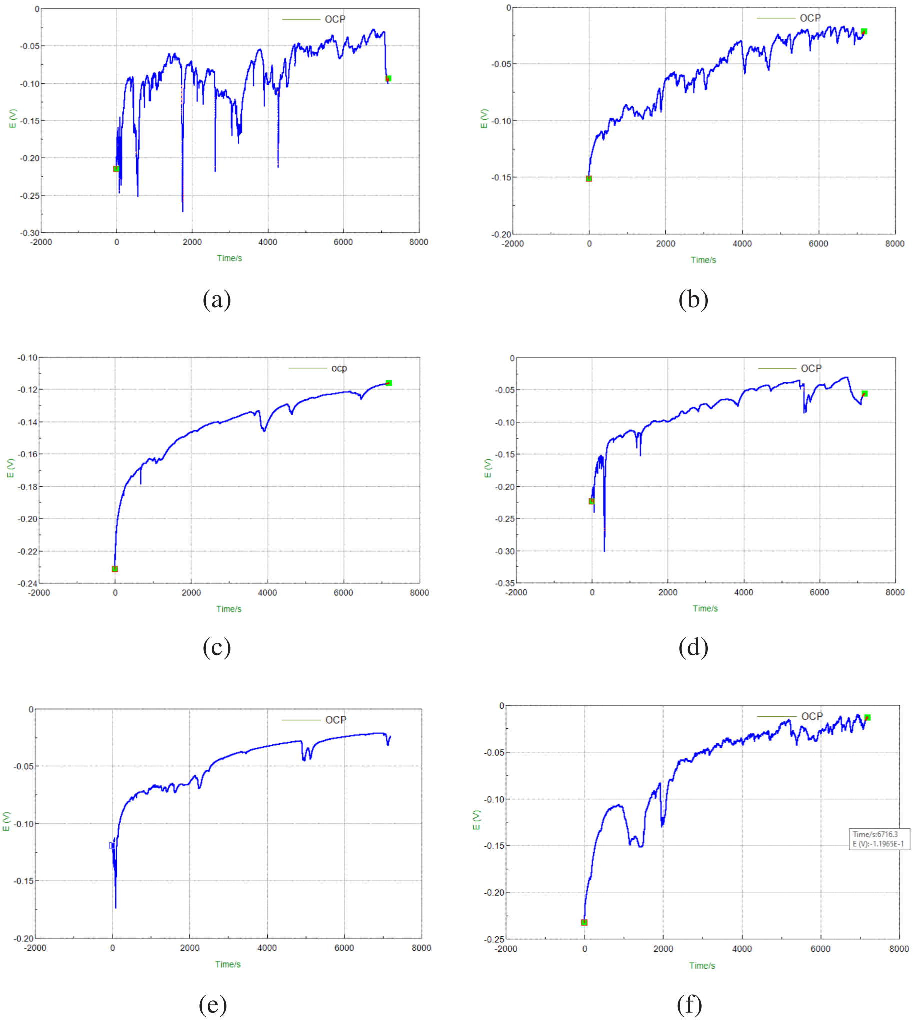

(a) (b)

(c) (d)

(e) (f)

Figure C.5: Open circuit potential plots of SLM-printed parts for 0.9M NaCl solution before heat treatment; a) 45°, b) 55°, c) 65°, d) 75°, e) 85°, f) 85°

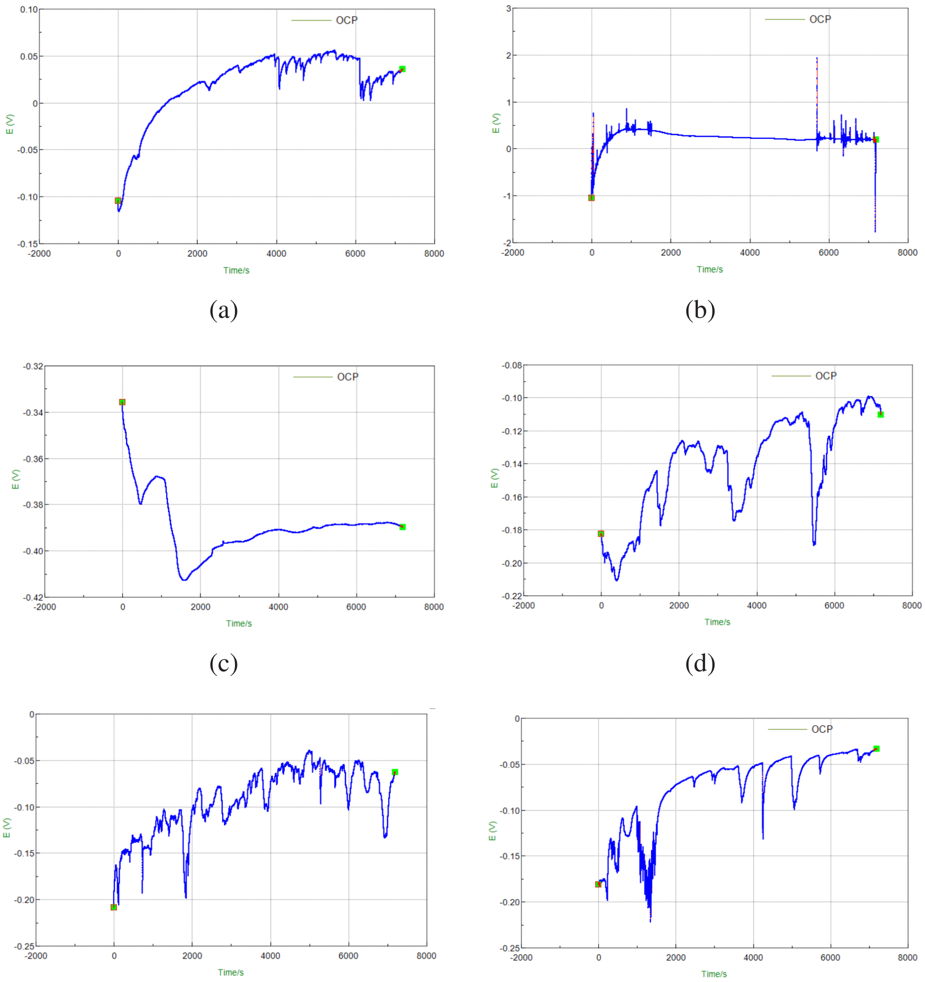

(a)

(b)

(c)

(d)

(e)

(f)

Figure C.6: Open circuit potential plots of SLM-printed parts for 3.5M NaCl solution before heat treatment; a) 45°, b) 55°, c) 65°, d) 75°, e) 85°, f) 85°

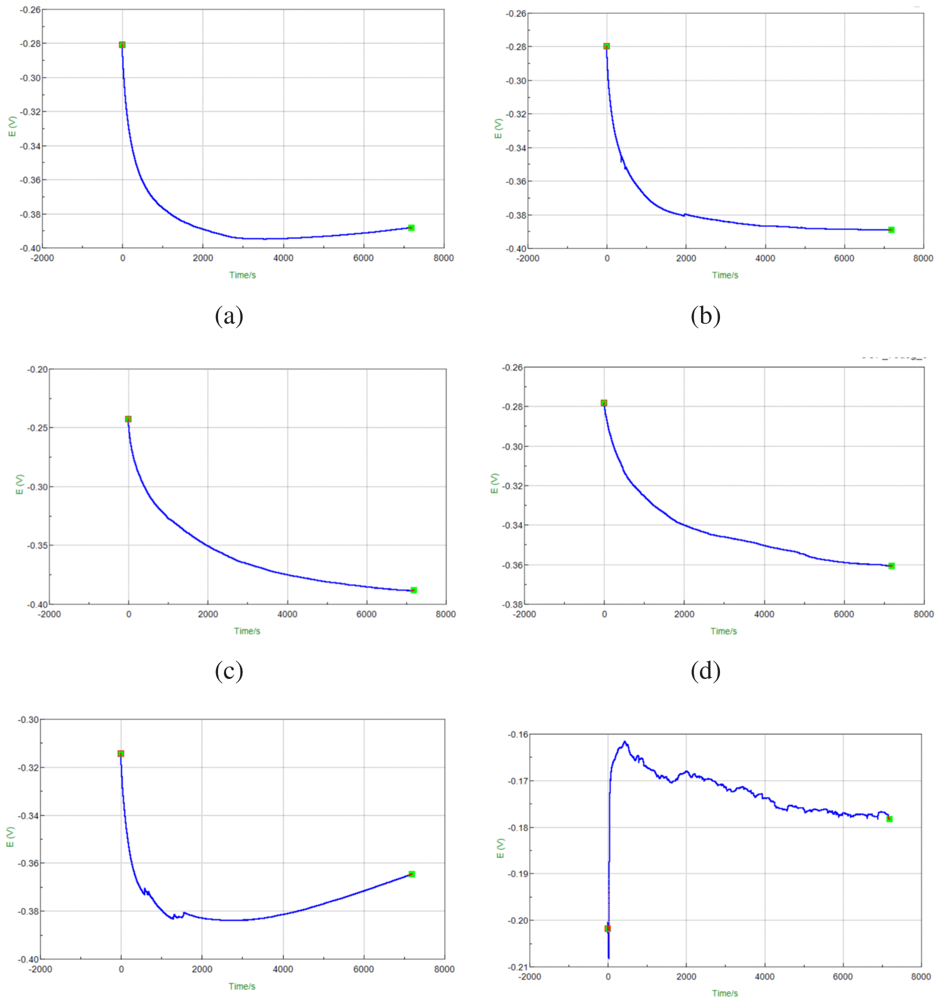

(a) (b)

(c) (d)

(e) (f)

Figure C.7: Open circuit potential plots of SLM-printed parts for 0.9M NaCl solution after heat treatment; a) 45°, b) 55°, c) 65°, d) 75°, e) 85°, f) 85°

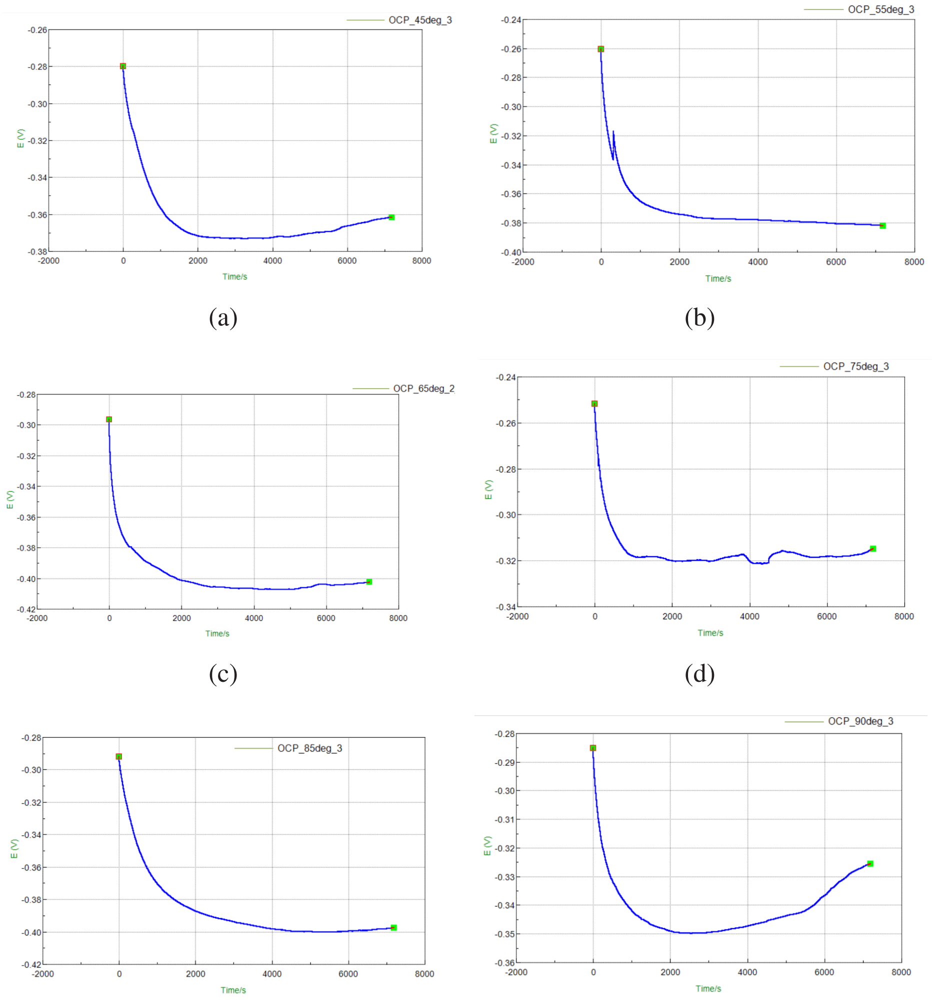

(a)
(b)
(c)
(d)
(e)
(f)

Figure C.8: Open circuit potential plots of SLM-printed parts for 3.5M NaCl solution after heat treatment; a) 45°, b) 55°, c) 65°, d) 75°, e) 85°, f) 85°